

Impulsive Electromagnetic Emission near a Black Hole

CHRISTOPHER THOMPSON¹

¹*Canadian Institute for Theoretical Astrophysics, 60 St. George St., Toronto, ON M5S 3H8, Canada.*

(Received 2018 October 31; Published 2019 March 20)

ABSTRACT

The electromagnetic signature of a point explosion near a Kerr black hole (BH) is evaluated. The first repetitions produced by gravitational lensing are not periodic in time; periodicity emerges only as the result of multiple circuits of the prograde and retrograde light rings and is accompanied by exponential dimming. Gravitational focusing creates a sequence of concentrated caustic features and biases the detection of a repeating source toward alignment of the BH spin with the plane of the sky. We consider the polarization pattern in the case of emission by the Lorentz upboosting and reflection of a magnetic field near the explosion site. Then the polarized fraction of the detected pulse approaches unity, and rays propagating near the equatorial plane maintain a consistent polarization direction. Near a slowly accreting supermassive BH (SMBH), additional repetitions are caused by reflection off annular fragments of an orbiting disk that has passed through an ionization instability. These results are applied to the repeating fast radio burst (FRB) source 121102, giving a concrete and predictive example of how FRB detectability may be biased by lensing. A gravitational lensing delay of 10–30 s, and reflection delay up to $\sim 10^4$ s, are found for emission near the innermost stable circular orbit of a $3 \times 10^5 M_{\odot}$ SMBH; these effects combine to produce interesting correlations between delay time and burst fluence. A similar repetitive pulse envelope could be seen in the gravitational wave signal produced by a collision between compact stars near a SMBH.

Keywords: black hole physics – dark matter – gravitational lensing – radiation mechanisms: nonthermal – relativity

1. INTRODUCTION

This article considers the impulsive injection of electromagnetic fields within a small volume next to a spinning black hole (BH). The radiation pattern at infinity shows a discrete time structure and forms a sequence of caustic features, which we describe along with the polarization pattern. Our focus is on emission by particles (or collisions between them) in orbits confined to the equatorial plane of the hole.

The signal from a continuously emitting point source orbiting a BH was first considered by [Cunningham & Bardeen \(1972\)](#) and has been analyzed subsequently by a number of authors: see [Broderick & Loeb \(2005\)](#), [Dokuchaev & Nazarova \(2017\)](#), and [Gralla et al. \(2018\)](#), and references therein. Continuous emission viewed at a large distance from the BH is strongly modulated at the orbital period

of the source, whereas, as we show, the signal of impulsive energy release develops periodicity only with some delay and with exponentially diminishing intensity.

In effect, we have mapped out the light-cone component of the electromagnetic Green function of a Kerr BH on the sphere at infinity, although only for a particular location and velocity of the source. The analogous problem of impulsive scalar field emission near a Schwarzschild BH has been treated by [Zenginoğlu & Galley \(2012\)](#) using a numerical relativity code, revealing a caustic structure identical to the one uncovered here in the zero-spin case. The simple ray-tracing method adopted here is more effective at extracting narrow temporal features in the extended signal and can easily incorporate propagation effects such as reflection. A much more elaborate caustic structure emerges when the BH spins, which complicates a direct comparison with the known spin-1 quasi-normal modes of a Kerr BH. The mapping of this caustic structure onto the observer’s plane for a continuously emitting point source of variable displacement from the BH was performed by [Rauch & Blandford \(1994\)](#) and [Bozza \(2008\)](#).

When a BH is a source of repeated point electromagnetic bursts, gravitational focusing creates a strong detection bias favoring the alignment of the BH spin with the plane of the sky. The repetitive pattern described here would also be imposed on the gravitational wave signal produced by a collision between neutron stars or stellar-mass BHs near a supermassive black hole (SMBH).

Part of the motivation for this study came from our proposal ([Thompson 2017a,b](#)) that fast radio bursts (FRBs) signal collisions between macroscopic dipolar dark matter particles and that repeating FRBs are powered by a small fraction of these particles that are captured by SMBHs into a dynamically cold ring close to the innermost stable circular orbit (ISCO). A few predictions of that model (strong linear polarization, extreme Faraday rotation, and strong high-frequency emission) are consistent with recent data collected from the only currently known repeating FRB 121102 ([Gajjar et al. 2018](#); [Michilli et al. 2018](#)). Measurements of time delays between successive bursts indicate a dearth of repetitions shorter than ~ 10 s, which is consistent with gravitational lensing by a $\sim 3 \times 10^5 M_{\odot}$ BH.

Electromagnetic bursts could be emitted over a range of frequencies, indeed with the emission peaking above 10-100 GHz in the aforementioned model. The escape of lower-frequency gigahertz waves from close to a SMBH requires the electron density to be low, less than $\sim 10^7 \text{ cm}^{-3}$ for FRB 121102 after taking into account the feedback of the strong electromagnetic wave on ambient electrons ([Thompson 2017b](#)). In that situation, a thin disk component of the accretion flow onto a SMBH will have passed through an ionization transition and frozen out, becoming susceptible to warping and breaking ([Nayakshin & Sunyaev 2003](#); [Nealon et al. 2015](#)). Especially for the BH spin orientation favored by lensing detection bias, specular reflection off this orbiting material is an additional source of repetitions over 10^{2-3} s intervals.

The plan of this article is as follows. Section 2 describes our handling of point emission and ray propagation in a Kerr spacetime. A Monte Carlo method is used to map the trapped and escaping rays and to determine the pattern of delayed pulses. As is shown in Section 3, pulse arrival times and fluences can be calculated over much longer delays in the case of equatorial rays by a simple application of Raychaudhuri’s equations. Section 4 shows how the detection volume of the pulses depends on the orientation of the observer relative to the equatorial plane of the BH. In Section 5 we turn to consider hydrodynamical effects, in particular the mass profile of a quiescent accretion disk that passes through an ionization transition, and the characteristic displacement of warps and

annular fragments of such a disk from the SMBH. Section 6 applies our results to the repeating FRB source 121102, and Section 7 summarizes. The appendices give further details and tests of our calculations, in particular demonstrating the equivalence of a global Monte Carlo calculation with the integration of the ray expansion along equatorial geodesics.

2. RAY EMISSION AND PROPAGATION

We consider the isotropic emission of photons (rays), concentrated at a single time, near a BH of mass M and angular momentum Ma . The Kerr line element, expressed in Boyer-Lindquist (B-L) coordinates,¹ is

$$\begin{aligned} ds^2 &= \tilde{g}_{tt} dt^2 + g_{\phi\phi} [d(\phi - \omega t)]^2 + g_{rr} dr^2 + g_{\theta\theta} d\theta^2 \\ &= -\frac{\Sigma\Delta}{A} dt^2 + \frac{A}{\Sigma} \sin^2 \theta [d(\phi - \omega t)]^2 + \frac{\Sigma}{\Delta} dr^2 + \Sigma d\theta^2. \end{aligned} \quad (1)$$

Here

$$\omega = -\frac{g_{t\phi}}{g_{\phi\phi}} = \frac{2Mar}{A} \quad (2)$$

is the angular frequency of a zero angular momentum observer (ZAMO), $\tilde{g}_{tt} \equiv g_{tt} - \omega^2 g_{\phi\phi}$, and $\Sigma(r, \theta) = r^2 + a^2 \cos^2 \theta$, $\Delta(r) = r^2 - 2Mr + a^2$, and $A(r, \theta) = (r^2 + a^2)^2 - a^2 \Delta \sin^2 \theta$. The asymptotic direction of escaping rays is recorded in colatitude and azimuth (θ, ϕ) .

Emission is assumed to take place in the frame of a massive particle moving in a prograde circular orbit of angular velocity

$$\omega_c = \frac{(Mr)^{1/2}}{r^2 + a(Mr)^{1/2}}. \quad (3)$$

We particularly explore emission at the ISCO, whose radius depends on the spin and mass of the hole (Bardeen et al. 1972)

$$\begin{aligned} r_{\text{isco}} &= M \left\{ 3 + Z_2 - [(3 - Z_1)(3 + Z_1 + 2Z_2)]^{1/2} \right\}; \\ Z_1 &\equiv 1 + (1 - a^2/M^2)^{1/3} [(1 + a/M)^{1/3} + (1 - a/M)^{1/3}]; \\ Z_2 &\equiv (3a^2/M^2 + Z_1^2)^{1/3}. \end{aligned} \quad (4)$$

For example, repeating FRB emission could arise from collisions between superconducting dipoles that gradually lose orbital energy by hydromagnetic dissipation, ending up in a dynamically cold ring near the ISCO of a SMBH (Thompson 2017a).

The photon wavevector in this emission frame has components k_{em}^a given by

$$k_{\text{em}}^{(1)} = k_{\text{em}}^{(0)} \sin \theta_{\text{em}} \cos \phi_{\text{em}}; \quad k_{\text{em}}^{(2)} = -k_{\text{em}}^{(0)} \cos \theta_{\text{em}}; \quad k_{\text{em}}^{(3)} = k_{\text{em}}^{(0)} \sin \theta_{\text{em}} \sin \phi_{\text{em}}. \quad (5)$$

Here θ_{em} and ϕ_{em} are angles on a small sphere surrounding the emission point, with $\theta_{\text{em}} = 0$ corresponding to the direction $-\hat{\theta}$, $\theta_{\text{em}} = \pi/2$, $\phi_{\text{em}} = 0$ to the direction \hat{r} , and $\theta_{\text{em}} = \pi/2$, $\phi_{\text{em}} = \pi/2$ to the direction $\hat{\phi}$. The ray tangent vector is related to the emission-frame wavevector by $dx^\mu/d\lambda = e_a^\mu k_{\text{em}}^a$,

¹ Unless otherwise indicated, we use geometrical units in which $c = G = 1$.

where λ is the affine parameter, and the tetrad

$$\begin{aligned} e_{(0)}^\mu \partial_\mu &= \frac{\gamma_{\text{em}}}{(-\tilde{g}_{tt})^{1/2}} \partial_t + \frac{\gamma_{\text{em}}(\beta_{\text{em}} + \beta_\omega)}{g_{\phi\phi}^{1/2}} \partial_\phi; \\ e_{(1)}^r &= g_{rr}^{-1/2}; & e_{(2)}^\theta &= g_{\theta\theta}^{-1/2} \\ e_{(3)}^\mu \partial_\mu &= \frac{\gamma_{\text{em}}\beta_{\text{em}}}{(-\tilde{g}_{tt})^{1/2}} \partial_t + \frac{\gamma_{\text{em}}(1 + \beta_{\text{em}}\beta_\omega)}{g_{\phi\phi}^{1/2}} \partial_\phi. \end{aligned} \quad (6)$$

Here

$$\beta_\omega = \frac{g_{\phi\phi}^{1/2}}{(-\tilde{g}_{tt})^{1/2}} \omega \quad (7)$$

and

$$\beta_{\text{em}} = \frac{g_{\phi\phi}^{1/2}}{(-\tilde{g}_{tt})^{1/2}} (\omega_c - \omega); \quad \gamma_{\text{em}} = (1 - \beta_{\text{em}}^2)^{-1/2} \quad (8)$$

is the boost connecting the ZAMO frame to the emission frame.

The electric vector of the emitted ray is determined by a simple geometrical model, which is based on the emission process described by [Rees \(1977\)](#) and [Blandford \(1977\)](#) in the context of BH evaporation, and is also one of the processes that can power radio emission from a tiny electromagnetic explosion ([Thompson 2017b](#)). Here an electrically conducting, spherical shell expands outward radially from the emission point. The ambient magnetic field (with direction \hat{B}_{ex} in the emission frame) is observed as a counter-propagating electromagnetic wave in the rest frame of the shell and, in the emission frame, is upboosted into a superluminal wave with unit electric vector $\hat{E} = -\hat{R}_{\text{em}} \times \hat{B}_{\text{ex}} / |\hat{R}_{\text{em}} \times \hat{B}_{\text{ex}}|$, where \hat{R}_{em} is the radial unit vector in the direction of expansion. We choose for calculational purposes a toroidal ambient magnetic field, $\hat{B}_{\text{ex}} = \pm \hat{\phi}$. The initial B-L frame polarization is then given by $\varepsilon_{\text{em}}^\mu = \pm e_a^\mu (\hat{R}_{\text{em}} \times \hat{\phi})^a / |\hat{R}_{\text{em}} \times \hat{\phi}|$.

Ray propagation is handled by evolving the geodesic equation

$$\frac{d^2 x^\mu}{d\lambda^2} = -\Gamma_{\alpha\beta}^\mu \frac{dx^\alpha}{d\lambda} \frac{dx^\beta}{d\lambda}. \quad (9)$$

The orbital energy and angular momentum integrals are

$$\begin{aligned} \mathcal{E} &= -g_{t\mu} \frac{dx^\mu}{d\lambda} = -\tilde{g}_{tt} \frac{dt}{d\lambda} + \omega \mathcal{L}_z; \\ \mathcal{L}_z &= g_{\phi\mu} \frac{dx^\mu}{d\lambda} = g_{\phi\phi} \left(\frac{d\phi}{d\lambda} - \omega \frac{dt}{d\lambda} \right), \end{aligned} \quad (10)$$

and are expressed in terms of emission-frame quantities by

$$\begin{aligned} \mathcal{E} &= (-\tilde{g}_{tt})^{1/2} \gamma_{\text{em}} \left[1 + \beta_{\text{em}}\beta_\omega + (\beta_{\text{em}} + \beta_\omega) \hat{k}^{(3)} \right] k_{\text{em}}^{(0)}; \\ \mathcal{L}_z &= g_{\phi\phi}^{1/2} \gamma_{\text{em}} (\beta_{\text{em}} + \hat{k}^{(3)}) k_{\text{em}}^{(0)}. \end{aligned} \quad (11)$$

Although the ray trajectory can also be obtained by quadrature, by combining \mathcal{E} and \mathcal{L}_z with the Carter constant (see [Frolov & Novikov 1998](#) and [Appendix A.3](#)), a direct integration of the

geodesic equation has several advantages: it allows one easily to include rays with turning points, to resolve delayed narrow pulses and construct maps, and to analyze correlations between variables (e.g. between winding number or time delay and the minimum approach to the BH). The integrations are easily accomplished to high accuracy ($\sim 10^{-12}$ or better) using a package such as DLSODE (Hindmarsh 1983).

The polarization 4-vector also evolves by parallel transport,

$$\frac{d\varepsilon^\mu}{d\lambda} = -\Gamma_{\alpha\beta}^\mu \frac{dx^\alpha}{d\lambda} \varepsilon^\beta. \quad (12)$$

One finds that ε^μ develops a longitudinal component parallel to k^μ , but the physical polarization is easily read off at large radius by truncating to the ϕ and θ components.

2.1. Absorption vs. Escape

The rays that are absorbed by the BH can be mapped out on a small sphere surrounding the emission point, defined by the angles (5). The result is shown in Figure 1 for a range of a/M . The angular zone of accreted rays grows in size with rising a/M as a result of the strengthening of spacetime curvature at the ISCO and the increasing apparent angular size of the hole. Rays propagating to the poles ($\theta_{\text{em}} = 0, \pi$) escape to infinity.

The net fraction of escaping rays, under the assumption of isotropic emission, is shown also as a function of the BH spin in Figure 1. In the case of anisotropic emission, this result would still apply after averaging over many explosions with random orientation.

2.2. Ray Intensity at Null Infinity

The distribution of rays across the sphere at infinity is compared in Figure 2 for various a/M . In a frame other than the emission frame – in particular the ZAMO frame – the surface density of rays is inhomogeneous on a small light sphere surrounding the emission point, being aberrated by a factor $\mathcal{D}_{\text{em}}^2 = \gamma_{\text{em}}^2 (1 + \hat{k}_{\text{em}}^{(3)} \beta_{\text{em}})^2$. One may define a ray ‘fluence’ in the case of point emission in time; at a small affine distance λ_0 from the emission point this is

$$\mathcal{F}_0 = \mathcal{D}_{\text{em}}^2 \frac{\mathcal{N}}{4\pi R_{\text{em},0}^2}; \quad R_{\text{em},0} = \lambda_0 (-\tilde{g}_{tt})^{1/2} \frac{dt}{d\lambda}. \quad (13)$$

In a Monte Carlo calculation, \mathcal{N} is simply the number of trial rays. The ray fluence on a sphere of large radius $r(\lambda) \gg M$ can be normalized to emission from a source at rest in flat space,

$$\frac{\mathcal{F}(\lambda)}{\mathcal{F}_{\text{flat}}(\lambda)} = \frac{\mathcal{D}_{\text{em}}^2}{\delta A_\perp / \delta A_{\perp,0}} \left[\frac{r(\lambda)}{R_{\text{em},0}} \right]^2. \quad (14)$$

Here, δA_\perp is the cross-sectional area of an infinitesimal ray bundle surrounding a given geodesic. The Monte Carlo result can be directly tested against an integration of Raychaudhuri’s equations; see Appendix B.

The cumulative Poynting flux transmitted over the small sphere in the ZAMO frame is related to the total energy $\mathcal{E}_{\text{em}} = k_{\text{em}}^{(0)} \mathcal{N}$ released in the emission frame by $\mathcal{F}_{\mathcal{E},0} = \mathcal{D}_{\text{em}} k_{\text{em}}^{(0)} \mathcal{F}_0$. The Poynting flux transmitted by a ray bundle to a large distance from the BH is obtained by multiplying by the energy integral (10), which is proportional to $k_{\text{em}}^{(0)}$ following Equation (11).

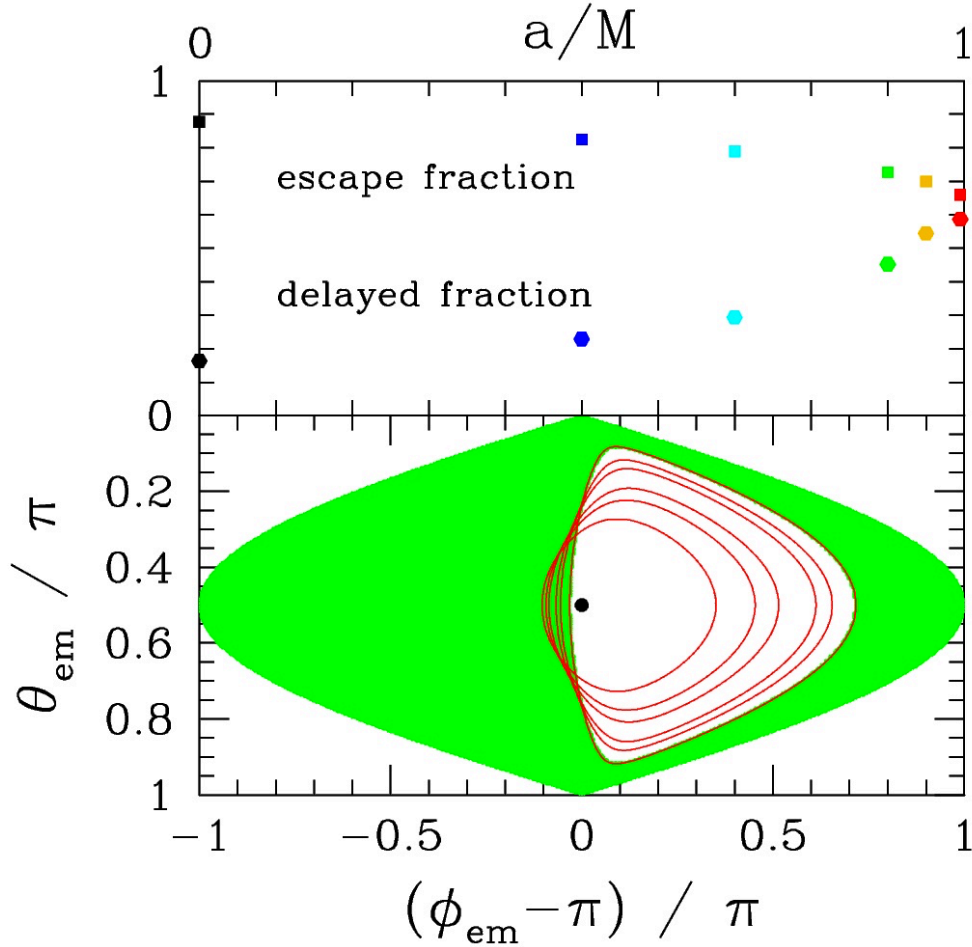


Figure 1. Bottom panel: trapped (white) and escaping (green) rays emitted by a spherical point flash from the ISCO of a Kerr BH with dimensionless spin $a/M = 0.99$, as mapped onto a small sphere co-orbiting with the point source (Equation (5)). Black dot denotes the direction of the center of the hole, with rays to the right being emitted against the orbital motion. Red lines show the boundary between trapped and escaping rays for a sequence of BH spins, $a/M = 0, 0.5, 0.7, 0.9, 0.95, 0.99$. Top panel: fraction of the escaping rays appearing in delayed pulses (hexagonal dots), and fraction of all rays escaping to infinity (square dots).

In the case of a nonspinning BH, gravitational lensing produces a strong intensity peak near the observer azimuth that is antipodal to the emission point, as well as a secondary peak that is shifted by 180° . The ray fluence near the main peak diverges as $\sim |\theta - \pi/2|^{-1}$ for low-to-moderate BH spin (Figure 3). One also observes in Figure 2 a broad Doppler shift in the intensity contours in the direction of orbital motion.

The primary caustic sits precisely at the antipodal point only for a nonspinning BH; differential frame dragging of prograde and retrograde rays shifts its position when $a > 0$, and the primary and secondary caustics move closer together. An infinite sequence of caustics is in fact present: the tertiary caustic aligns with the primary caustic when $a = 0$. A similar effect was observed by Zenginoglu &

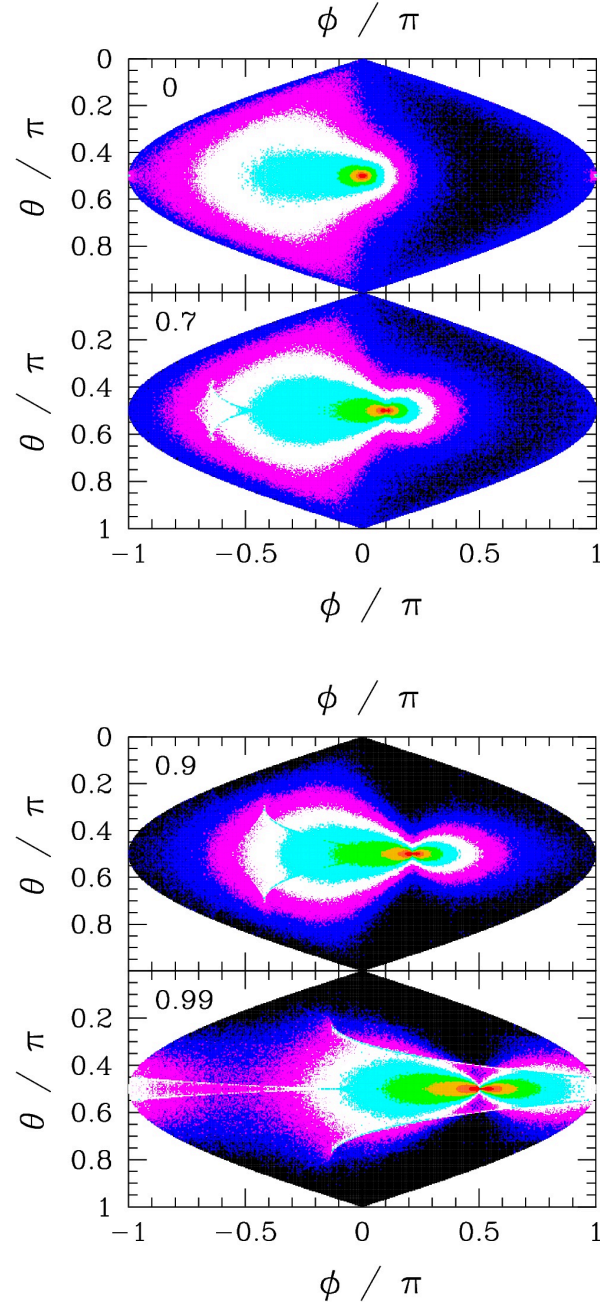


Figure 2. Ray fluence (defined by Equation (14)) on the sphere at infinity, corresponding to point emission in the frame of a massive test particle on the ISCO of a Kerr BH. The BH spin increases from top to bottom: $a/M = 0, 0.7, 0.9, 0.99$. Colors mark zones with fluence separated by powers of 1.7 (1.8 bottom panel), increasing from black to blue, mauve, white, cyan, green, gold, and red. The point ($\theta = 0, \phi = 0$) is antipodal to the position of the explosion. Strong peak near the center is produced by gravitational lensing, and the broad concentration to its left is caused by the motion of the emission frame. Projection is equal area, with horizontal lines marking constant rotational colatitude θ . These maps are obtained by a Monte Carlo procedure involving 10^{23} trial rays, whose asymptotic direction is recorded in pixels of size $(2^{-8}\pi, 2^{-8}\pi/\sin\theta)$.

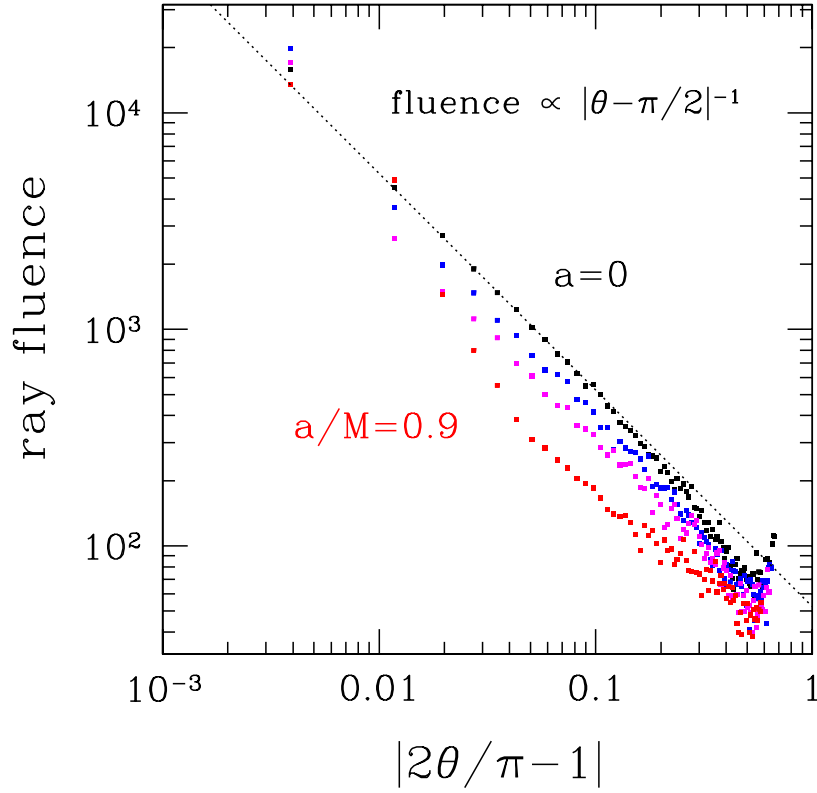


Figure 3. Dependence of ray fluence on latitude above and below the equatorial caustic on the sphere at infinity, as seen in Figure 2. BH spins range from $a = 0$ (black points) to $a/M = 0.9$ (red points). Angular dependence is $|\theta - \pi/2|^{-1}$ in the simplest case of a non-spinning BH (dotted line).

Galley (2012) in a numerical evolution of point scalar field emission near a Schwarzschild BH. Figure 4 demonstrates this effect for nearly equatorial rays.

Here we also plot the energy fluence at null infinity in the case $a = 0$. The fluence transported by successive impulses decays in precisely the manner expected for the lowest radial order spin-1 quasi-normal mode: the top-left panel of Figure 4 shows a decay factor equal to $e^{-2\omega_I t_{\text{ring}}} = 1/420$, where $\omega_I = 0.1850/2M$ is the imaginary part of the mode frequency (Berti et al. 2009), and $t_{\text{ring}} = 2\pi \cdot 27^{1/2} M$ is the orbital period of the light ring. By contrast, when the BH spins, the fluence received by a fixed observer is aperiodically biased by the intervention of caustic features, which complicates a comparison with the quasi-normal mode. Further details of the time profile of the delayed pulses are described in Section 2.3.

The polarization pattern at infinity is shown, at a somewhat lower resolution, in Figure 5. One observes that the electric vector maintains a nearly uniform direction near the rotational equator, excepting for observers oriented close to the main intensity cusp. The deflection of the polarization

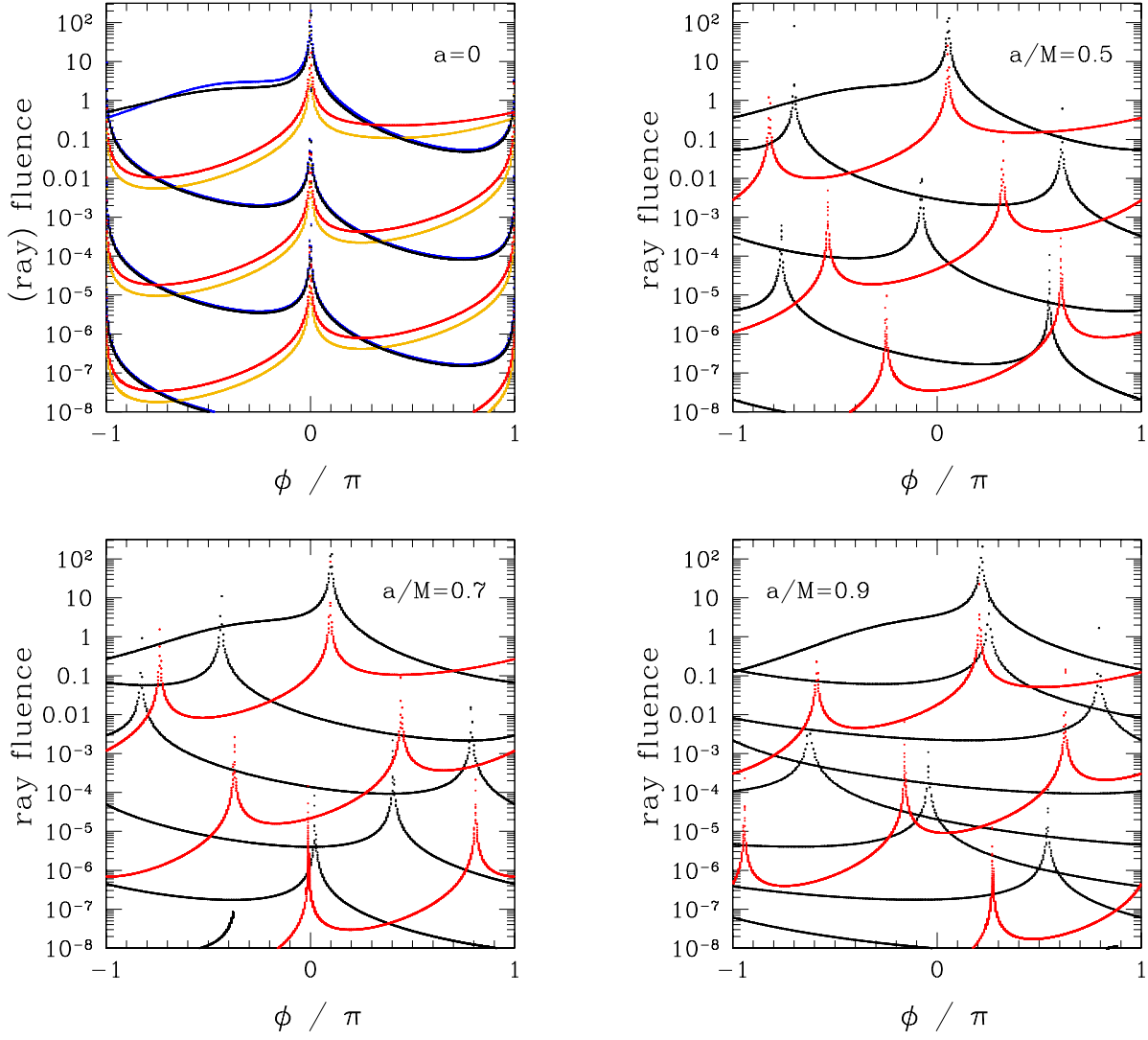


Figure 4. Black and red curves: ray fluence versus azimuth, as measured on the equatorial plane of the BH at null infinity. BH spin increases from the top left. Blue and gold curves: corresponding energy fluence after weighting by the energy integral (11). First pulse detected by an observer sitting at angle ϕ corresponds to the top black/blue curve to the left of the top caustic, and the top red/gold curve to the right. Successive pulses of diminishing fluence are emitted at increasing times; see also Figure 10. When $a > 0$, the successive caustics shift in angle because of the differing periods of the prograde and retrograde light rings and the transit times of polar rays. These curves are obtained by integrating the Raychaudhuri equations (17) for a large number of equatorial rays. In the cases with higher spins, the contribution from polar wavefronts connecting the caustic points is missing (see Figure 7).

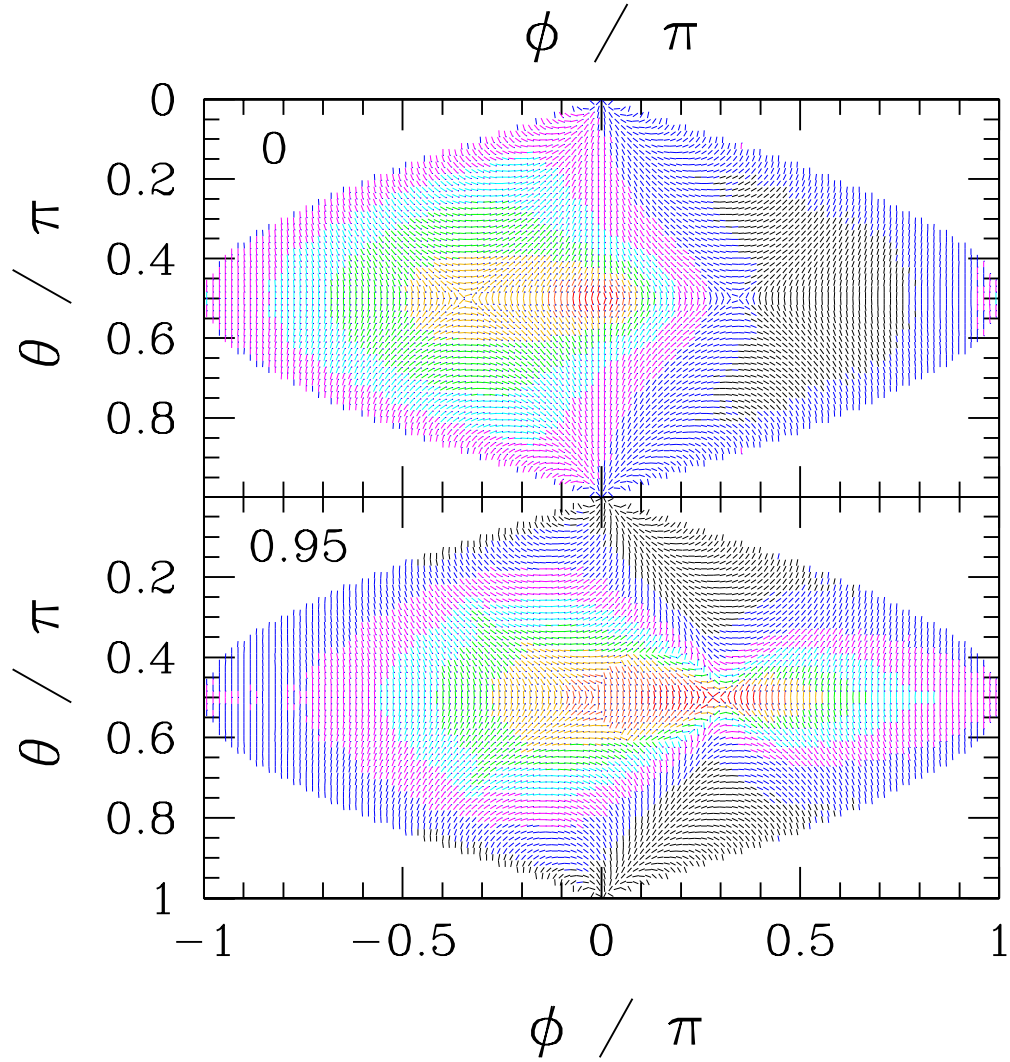


Figure 5. Linear polarization pattern at null infinity, corresponding to emission by the upboosting and reflection of the ambient toroidal magnetic field near the emission point. Top panel: $a = 0$; bottom panel: $a/M = 0.95$. Color zones are once again separated by powers of 1.5 (1.7 bottom panel) in intensity. A relatively uniform polarization pattern is seen near the BH equator, and also extending above and below the primary caustic for moderate BH spin. A differing magnetic configuration at the ISCO (e.g. a poloidal magnetic field) would imply a systematic rotation of the polarization, but the uniformity in the equatorial polarization pattern would be maintained. These maps are obtained by a Monte Carlo procedure, but now with angular resolution 4 times coarser than in Figure 2.

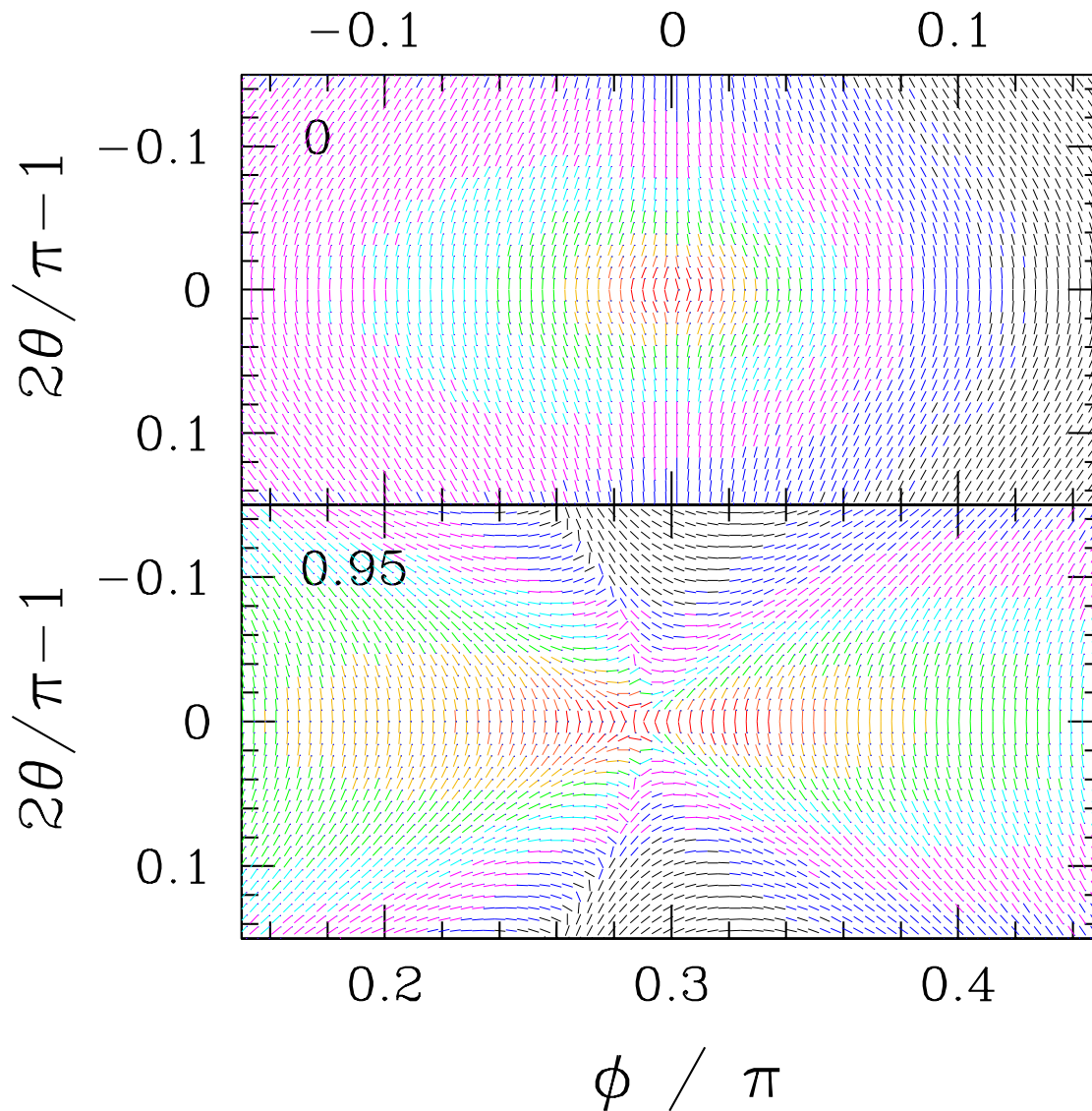


Figure 6. Same as Figure 5, but now showing a close up of the polarization pattern near the primary caustic, with the same angular resolution as in Figure 2.

angle near the cusp is shown in more detail in Figure 6, showing how it strengthens with growing BH spin.

2.3. Pattern of Delayed Pulses: Equatorial vs. Polar Rays

The zero of time is adjusted, independently for each observer direction, to the arrival of the initial impulse. The sequence of arriving pulses seen by observers aligned with the BH equator, at random values of ϕ relative to the emission point, is shown in Figure 7. The initial pulse connects at a particular azimuth with delayed equatorial rays (black and red curves) and at a slightly different azimuth with a narrow bundle of polar rays (green and cyan curves). This confluence of equatorial and polar rays coincides with the first, brightest caustic (Figure 2). The same phenomenon is repeated for the delayed pulses. However, as the BH spin grows, the rays reaching away from the equator (the green and cyan curves) grow in azimuthal extent: they connect separate caustic features on the prograde and retrograde rays that are offset from each other in azimuth (compare Figure 4).

Except for a nonspinning BH, the prograde (black) and retrograde (red) delayed pulses show different periods, which match the orbital periods of prograde and retrograde equatorial photon orbits (e.g. $2\pi \cdot 27^{1/2} M \simeq 32.6 M$ in the Schwarzschild case). This is confirmed by plotting the relation between delay time and winding angle or the minimum approach of the ray to the BH (Figure 8). Rays that closely approach one of the light rings experience a single radial bounce ($dr/d\lambda = 0$).

For larger BH spins, a larger fraction of rays also arrive in delayed pulses, especially those rays propagating near the BH equator (Figure 9).

3. DEFOCUSING OF EQUATORIAL RAYS

Equatorial rays offer more extensive and detailed information about the delayed light pulses produced by a point explosion than can be obtained with a brute force Monte Carlo procedure. Near the BH equator, it is simple to follow the ray expansion through turning points near one of the light rings. A comparison between the results of the two methods also provides a sharp test of both (Appendix B).

The Raychaudhuri equations simplify for equatorial null geodesics. We work with a tetrad e_A^μ that projects four-dimensional coordinates x^μ onto a transverse 2×2 dimensional space labeling the physical polarization degrees of freedom. The ray shear tensor $B_{AB} = e_A^\mu e_B^\nu \nabla_\mu k_\nu$ is decomposed into an isotropic expansion $\theta = d \ln \delta A_\perp / d\lambda = \delta^{AB} B_{AB}$ (where δA_\perp is the cross section of a narrow ray bundle) and a trace-free component $\sigma_{AB} = \frac{1}{2}(B_{AB} + B_{BA} - \theta \delta_{AB})$. Near the emission point on the ISCO, the off-diagonal components of B_{AB} vanish, and so the rotation can be set to zero along the ray. In the case of an equatorial geodesic, the off-diagonal components of σ_{AB} vanish exactly by symmetry. Then the (upper) diagonal component σ_+ evolves along with the expansion as (Poisson 2004)

$$\begin{aligned} \frac{d\theta}{d\lambda} &= -\frac{1}{2}\theta^2 - 2\sigma_+^2; \\ \frac{d\sigma_+}{d\lambda} &= -\theta\sigma_+ - R_{\alpha\mu\beta\nu} k^\alpha e_1^\mu k^\beta e_1^\nu \equiv -\theta\sigma_+ - C_+. \end{aligned} \quad (15)$$

Here the polarization tetrad must be parallel propagated along the ray, $de_A^\mu/d\lambda = -\Gamma_{\alpha\beta}^\mu e_A^\alpha dx^\beta/d\lambda$. A small affine distance λ_0 from the emission point, the expansion is initialized as $\theta = 2/\lambda_0$. The

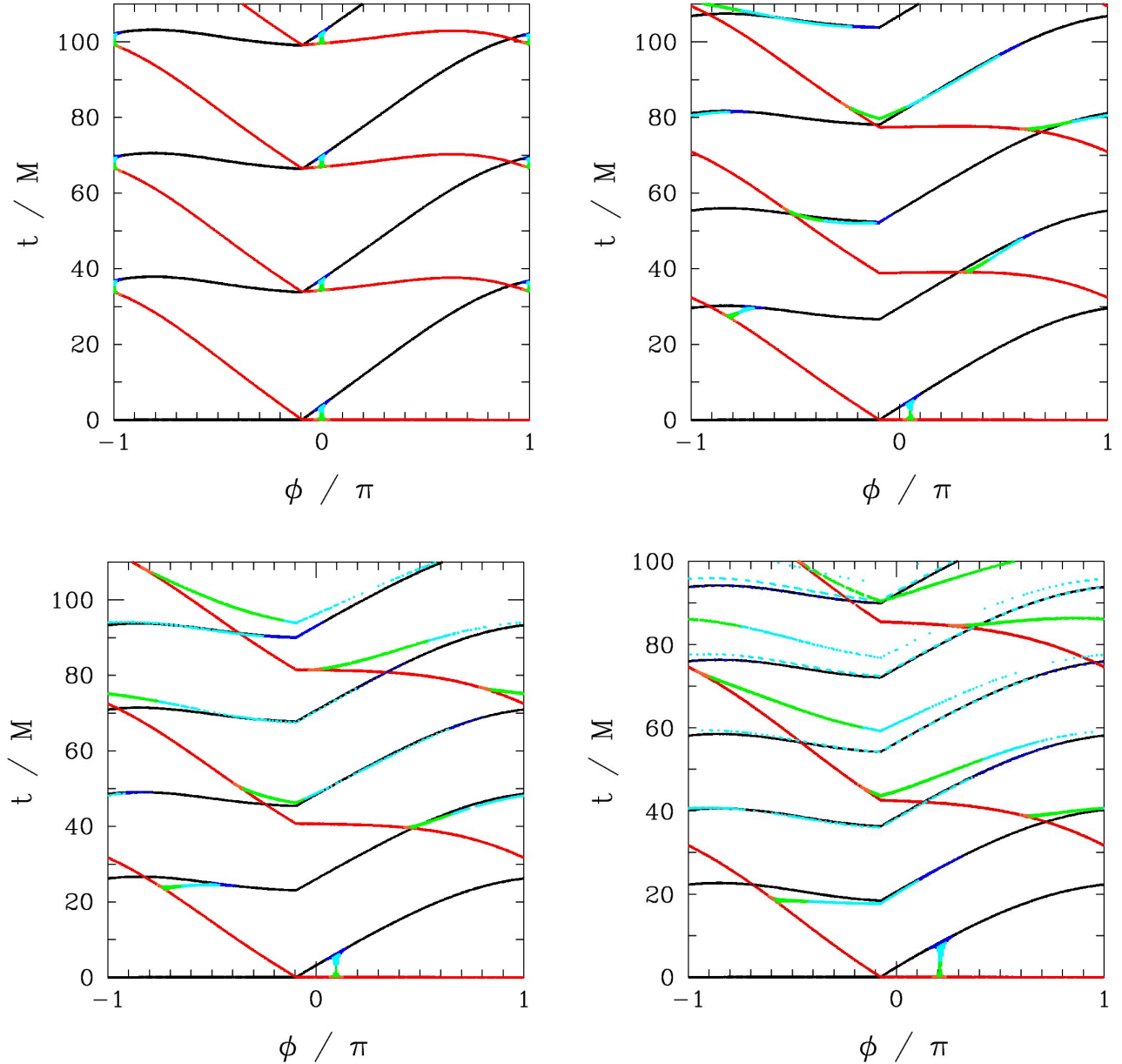


Figure 7. Pulse arrival times as a function of the azimuth of an observer positioned near $\theta = \pi/2$ at a large distance from the BH. Angle $\phi = 0$ is antipodal to the emission point on the ISCO. Top left panel: $a = 0$; top right panel: $a/M = 0.5$; bottom left panel: $a/M = 0.7$; bottom right panel: $a/M = 0.9$. In all cases the zero of time is shifted to the first pulse detected at a given observing angle. Black (red) lines denote prograde (retrograde) rays, which remain confined to $|\cos\theta| < 0.1$ from the emission point all the way to infinity. The periods of the respective light rings are clearly visible. Blue and cyan denote prograde rays with $0.1 < |\cos\theta|_{\max} < 0.5$ and $|\cos\theta|_{\max} > 0.5$; orange and green denote the corresponding retrograde rays. When a/M is small, most of the delayed pulses detected by an equatorial observer follow nearly equatorial geodesics, with the exception of caustic features associated with narrow azimuthal bundles of rays that reach close to the poles. The azimuthal range of the polar rays broadens with growing a/M ; comparison with Figure 4 shows that the caustics still coincide with the connections of the cyan/green and black red curves.

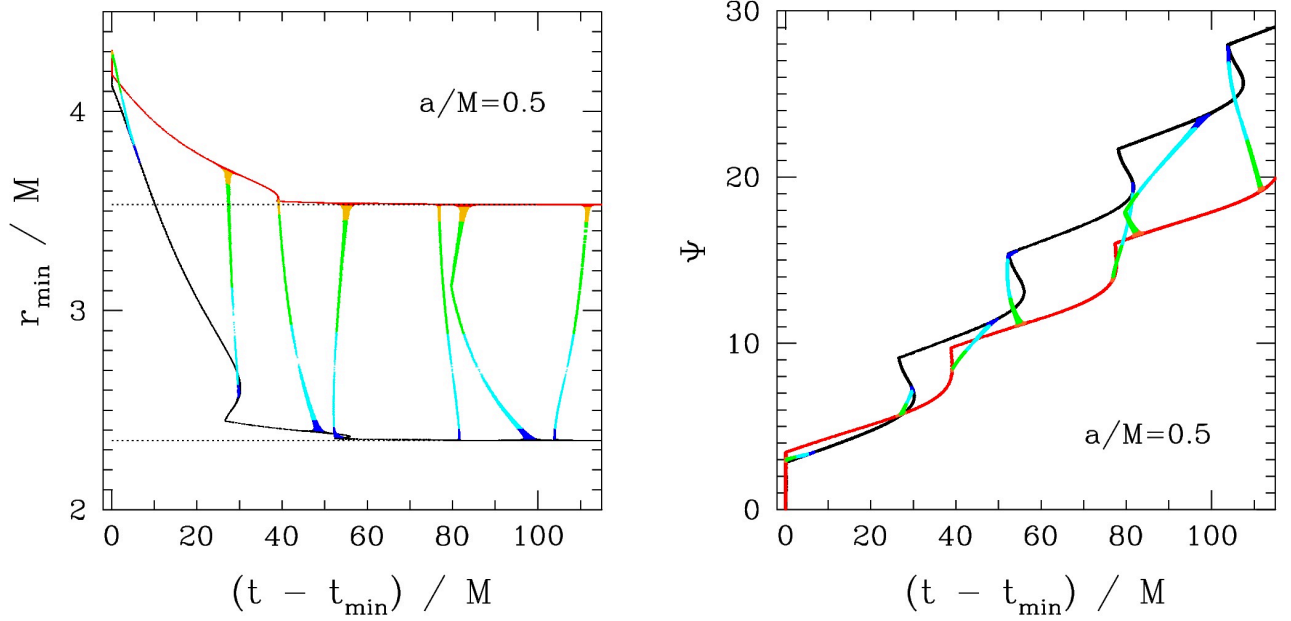


Figure 8. Left panel: minimum approach of a ray to the BH versus delay time from the first detected pulse, as seen on the BH equator ($\theta = \pi/2$). Color scheme is the same as in Figure 7. Black/red points: prograde/retrograde rays; blue/cyan/green/gold points denote rays reaching $|\cos\theta| > 0.1$. Horizontal dotted lines mark the prograde and retrograde photon orbits, here for $a/M = 0.5$. Right panel: winding angle of the ray around the BH. Rays that closely approach one of the light rings experience a single radial bounce ($dr/d\lambda = 0$).

polarization is initialized in the emission frame as

$$\begin{aligned} e_1^{(i)} &= -(\hat{k}_{\text{em}} \times \hat{\theta})^{(i)} / |\hat{k}_{\text{em}} \times \hat{\theta}|; \\ e_2^{(i)} &= (\hat{k}_{\text{em}} \times \vec{e}_1)^{(i)}, \end{aligned} \quad (16)$$

where $\hat{k}_{\text{em}}^{(i)} \equiv k_{\text{em}}^{(i)} / k_{\text{em}}^{(0)}$, and then transformed into the B-L frame using Equation (6), $e_A^\mu = e_a^\mu e_A^a$. The equations (15) may be combined to give

$$\frac{d^2 y_\pm}{d\lambda^2} = \mp C_+ y_\pm; \quad y_\pm(\lambda, \lambda_0) \equiv \exp \left[\frac{1}{2} \int_{\lambda_0}^{\lambda} (\theta \pm 2\sigma_+) d\lambda' \right]. \quad (17)$$

After integrating these equations along an equatorial ray, one obtains the expansion

$$\frac{\delta A_\perp(\lambda)}{\delta A_\perp(\lambda_0)} = \text{abs}(y_+ y_-). \quad (18)$$

The ray fluence at null infinity may then be compared with the result for emission by a stationary source in flat space using Equation (14).

The ray fluence is plotted for a large number of randomly chosen equatorial rays in Figure 4 (as a function of the relative azimuth of the observer) and in Figure 10 (as a function of the arrival time of the pulse). One sees that light pulses delayed by successive circuits of the BH form a caustic at the

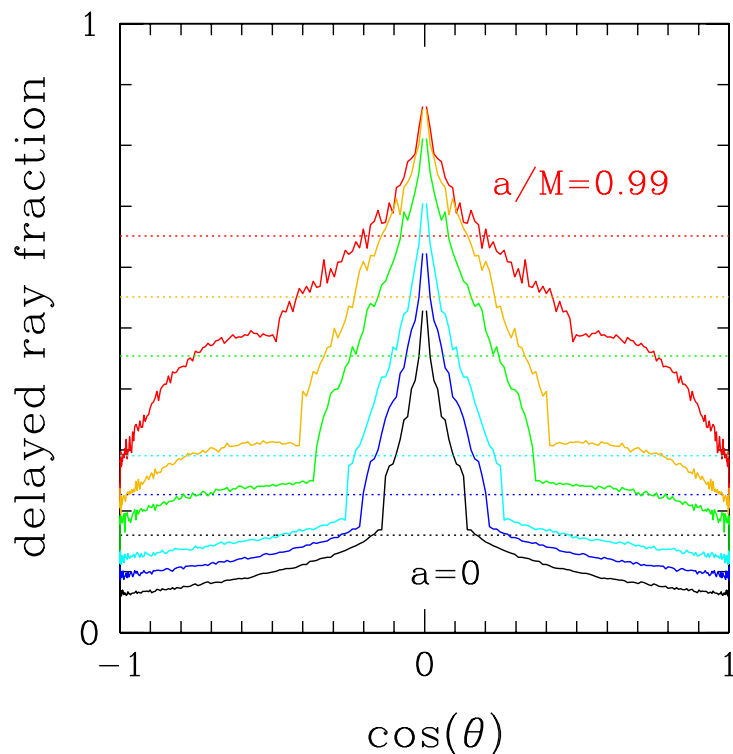


Figure 9. Solid lines: fraction of rays arriving in delayed pulses, as a function of colatitude θ measured on the sphere at infinity, for a range of BH spins ($a/M = 0, 0.5, 0.7, 0.9, 0.95, 0.99$, bottom to top). Dotted horizontal lines: fraction of rays arriving in delayed pulses, averaged over colatitude. The ray fluence is weighted more strongly to the equator for higher a/M , hence each dotted line is not a direct θ -average of the corresponding solid line.

same value of ϕ only in the case of vanishing BH spin. Otherwise, the prograde and retrograde light-ring periods differ from each other and from the transit times of polar rays, so that the successive caustics shift in phase.

4. LENSING BIAS: DETECTION RATE VS. BH ORIENTATION

Consider now the possibility that repeated electromagnetic point explosions occur close to the ISCO of a BH. This is the case in the model of FRBs described in [Thompson \(2017a,b\)](#). Here an observer aligned with the BH equator ($\theta = \pi/2$) will see on occasion a very bright pulse, when the emission point lies diagonally opposite to the observer's direction. If the explosion energy is limited to some maximum value (as it is in the model just described, as determined by the mass of annihilating dark matter particles), then a radio telescope will be sensitive to emission from a much greater volume when the BH spin is aligned with the plane of the sky, as compared with emission from a BH with a more randomly directed spin. [Figure 11](#) shows that the detection volume in Euclidean space has a strong spike at $\theta = \pi/2$.

Observers with this favored orientation also see a more consistent polarization signature. The emission process we consider (upboosting of an ambient magnetic field by a tiny explosion) produces

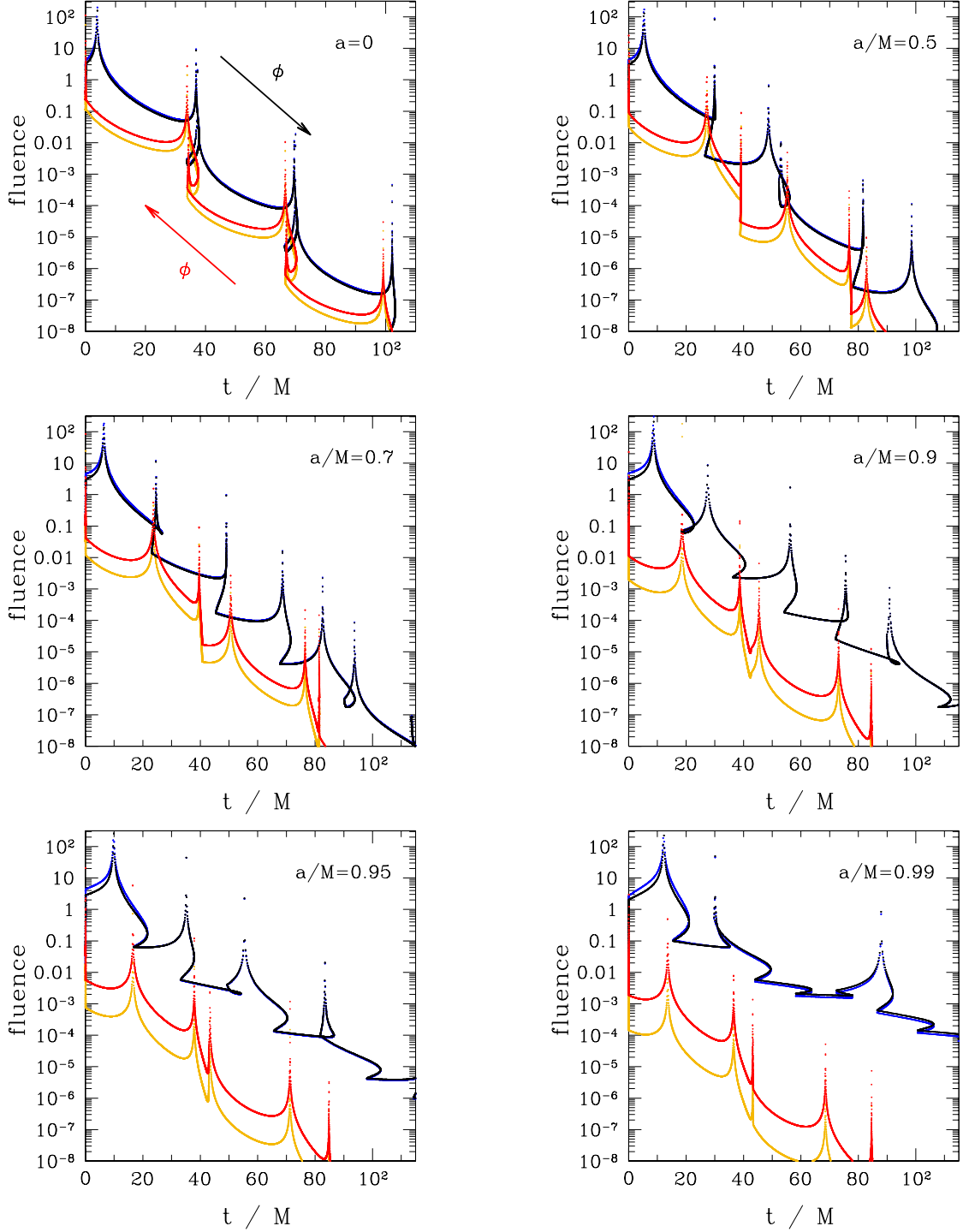


Figure 10. Same as Figure 7, but now fluence vs. time, for observers positioned at colatitude $\theta = \pi/2$. Black/red points show the prograde/retrograde ray fluence and track the corresponding curves on the t - ϕ plot, with angles $\phi = -\pi$ and π identified. Blue and gold points show the energy fluence, weighted by the energy integral of each ray.

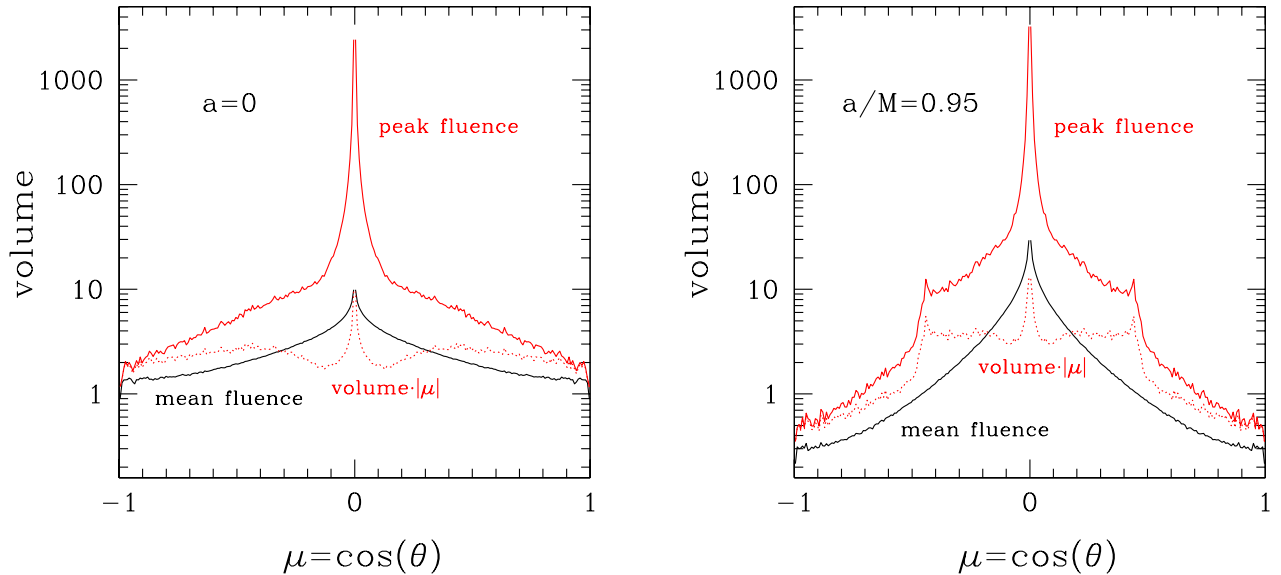


Figure 11. Normalized euclidean volume V corresponding to a fixed threshold pulse fluence, as detected by an observer at fixed BH latitude. Black curve: fluence is averaged over successive pulses emitted at random orbital phase with respect to the observer. Red curve: volume corresponding to the peak fluence detected at a given latitude. The cutoff in volume (and fluence) at $\mu = 0$ is an artifact of the finite size of the angular grid used to map outgoing rays. Dotted curve: differential volume $V \cdot \mu$. Left panel: $a = 0$; right panel: $a/M = 0.95$.

a high degree of linear polarization when the damping length of the impulse is small compared with r_{isco} . Figure 12 shows the variance in the polarization angle, over successive releases of energy at random orbital phases, as a function of the latitude of the observer. This variance is minimized just where the detection volume is maximized. The implications of these results for the repeating burst emission of FRB 121102 are discussed in Section 6.

4.1. Variation in the Explosion-BH Separation

Although emission near the ISCO is a direct consequence of the model for FRBs that motivates our calculations, it is worth briefly considering the possibility of larger separations between the emission radius r_{em} and the BH. For example, collisions between two compact stars are most likely to occur well outside the ISCO, and so a distant observer will have a smaller probability of seeing a strong gravitational lensing signature imposed on the gravity waveform.

The proportion of rays captured into the light ring, and subsequently released in caustics of secondary or higher degree, would decrease as $\sim 1/r_{\text{em}}^2$. The brightness of the primary caustic, as measured at a fixed angular displacement $\alpha_{\text{obs}} = |\theta_{\text{obs}} - \pi/2|$ of the observer from the BH equator, is easily worked out in the weak-gravity regime. The fluence measured by an observer positioned at a distance r is proportional to the magnification. This is $\theta_E/2\theta_{\text{em-BH}}$ (e.g. Weinberg 2008), where $\theta_E \simeq (4Mr_{\text{em}})^{1/2}/r$ is the angular radius of the Einstein ring that would be observed at $\alpha_{\text{obs}} = 0$, and $\theta_{\text{em-BH}} \ll \theta_E$ is the angle between the direct lines from the emission point and from the BH to

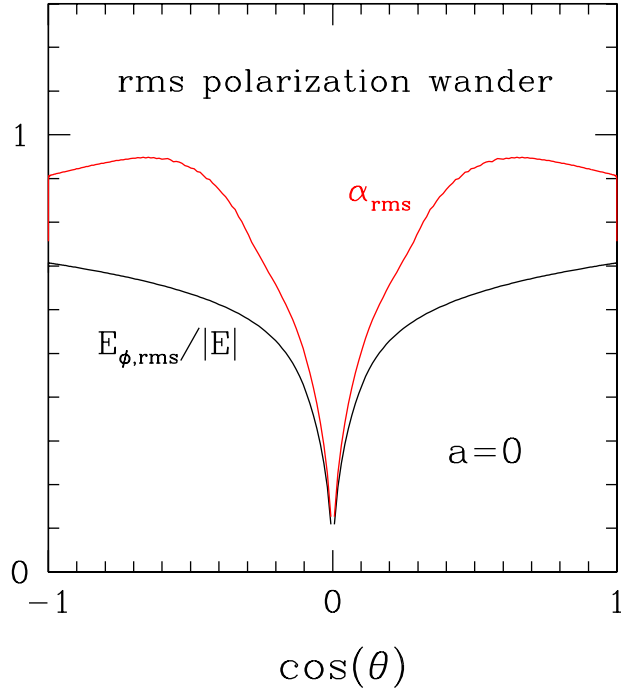


Figure 12. Red curve: rms variation in the linear polarization angle of the prompt electromagnetic pulse, as seen by an observer positioned at a fixed latitude but random orbital phase relative to the emission point. Black curve: rms ϕ component of the electric vector, also averaged over the angle ϕ of emission. Polarization variance is minimized where detection volume is maximized (Figure 11).

the observer. The latitude α_{obs} of the observer is related to θ_{em-BH} by $\alpha_{obs} = (r/r_{em})\theta_{em-BH}$. Hence the measured fluence is enhanced by a factor $\alpha_{obs}^{-1}(M/r_{em})^{1/2}$, precisely the angular scaling that is measured in Figure 3. A randomly positioned observer has a probability $\sim M/4r_{em}$ of seeing a strong lensing signature when $r_{em} \gg M$.

5. REFLECTION OFF QUIESCENT, COOL GAS

Although radio telescopes are relatively sensitive to transient phenomena, as measured by the electromagnetic energy received, the detection of low-frequency emission may be severely limited by absorption near the source (Pacholczyk 1970). A SMBH must sustain a very low accretion rate for gigahertz waves to escape from close to its horizon, even after allowing for the feedback of a strong electromagnetic wave on ambient electrons (Thompson 2017b). If a thin disk component of the accretion flow is present, the mass flow through it must also be substantially diminished. However, in contrast with a hot and dilute accretion component, a cool disk would still present a barrier to the propagation of low-frequency waves and an additional source of repetitions through reflection.

The behavior of a quiescent disk is more complicated than the lensing effects we have investigated so far, but some progress is possible in constraining the disk profile following an ionization transition. If the mass transfer rate \dot{M}_d through the disk drops far enough, the temperature at the disk midplane will reach $\sim 10^4$ K, below which the ionization level collapses. Then the magnetic field decouples

from the disk material, mass transfer driven by the magnetorotational instability essentially halts, except possibly in a thin surface layer (Gammie 1996), and the disk mass profile freezes. Such a cool, remnant disk has been hypothesized to orbit the SMBH near the Galactic center (Nayakshin & Sunyaev 2003). In the extreme environment of a SMBH, a surface layer should remain ionized by UV radiation and energetic particles, providing a mirror for a strong electromagnetic wave.

This disk is light enough to remain gravitationally stable, but outside a certain distance from the SMBH, its self-gravity is strong enough for the disk to withstand warping by the differential rotation of the Kerr spacetime. Close to the hole, the Lense-Thirring torque overwhelms internal disk stresses, and the disk normal aligns with the BH spin (Bardeen & Petterson 1975). Near the transition between these two regimes, which we now consider, the disk may break (Nealon et al. 2015).

The disk surface mass density Σ is well constrained following the ionization transition. The mass transfer rate toward a SMBH of mass M_\bullet is expressed dimensionlessly as a fraction \dot{m} of the value that will source an Eddington-level dissipative luminosity in the inner disk, $\varepsilon_{\text{rad}} \dot{M}_{\text{edd}} c^2 = 4\pi G M_\bullet m_p c / \sigma_T$. (Here ε_{rad} is the radiative efficiency in the inner disk, and the other constants have their usual meanings.) The $r - \phi$ component of the internal stress (considered here at the onset of the ionization transition) is expressed in terms of a viscous stress feeding off the radial differential rotation and is normalized to a fraction α of the gas pressure, $-\nu \rho R d\Omega/dR = \alpha P$. Given that the mass transfer rate drops gradually, it can be approximated by the steady-state formula (Pringle 1981)

$$\dot{M}_d = 3\pi\nu\Sigma = 2\pi\alpha\Omega h^2\Sigma = \frac{\dot{m}}{\varepsilon_{\text{rad}}} \frac{4\pi G M_\bullet m_p}{\sigma_T c} \quad (19)$$

at a cylindrical radius $R \gg R_g \equiv GM_\bullet/c^2$. The vertical scale height is expressed in terms of the orbital angular velocity, midplane temperature, and mean molecular weight as $h = \Omega^{-1}(k_B T_c / \mu)^{1/2}$.

Vertical radiative energy transfer is mediated by absorption, with opacity near the hydrogen ionization threshold

$$\kappa(P, T) = \kappa_0 T^{-\alpha} P^\beta. \quad (20)$$

Here, κ , temperature T and P are expressed in cgs units, and $\kappa_0 = 10^{12.026}$, $\alpha = 3.36$, and $\beta = 0.928$ (Zhu et al. 2009). The energy flux through each face of the disk (at a height $z \sim h$ above the midplane) is

$$\frac{3\Omega^2}{8\pi} \dot{M} = -\frac{1}{\kappa\rho} \frac{d}{dz} \left(\frac{4}{3} \sigma_{\text{SB}} T_c^4 \right) \sim \frac{8\sigma_{\text{SB}} T_c^4}{3\kappa(T_c, P_c)\Sigma}. \quad (21)$$

The midplane gas pressure and disk surface density are related to the midplane density ρ_c and scale height by $P_c = \rho_c(\Omega h)^2$ and $\Sigma \sim 2h\rho_c$. Then Equations (19)-(21) yield two expressions for ρ_c and T_c , which combine to give

$$T_c(R) = 3 \times 10^7 (\alpha M_{\bullet,6})^{-0.22} \left(\frac{\dot{m}}{\varepsilon_{\text{rad}}} \right)^{0.33} \left(\frac{R}{R_g} \right)^{-0.83} \text{ K}, \quad (22)$$

and

$$\Sigma(R) = 2 \times 10^6 \alpha^{-0.78} M_{\bullet,6}^{0.22} \left(\frac{\dot{m}}{\varepsilon_{\text{rad}}} \right)^{0.67} \left(\frac{R}{R_g} \right)^{-0.67} \text{ g cm}^{-2}. \quad (23)$$

Here the SMBH mass is normalized as $M_\bullet = M_{\bullet,6} \times 10^6 M_\odot$.

The ionization transition ($T_c \leq 1 \times 10^4$ K) occurs at an accretion rate

$$\frac{\dot{m}}{\varepsilon_{\text{rad}}} = 1 \times 10^{-3} (\alpha M_{\bullet,6})^{0.67} \left(\frac{R}{10^3 R_g} \right)^{2.5}, \quad (24)$$

when the surface density has dropped to

$$\Sigma(R) = 3 \times 10^2 \alpha^{-0.33} M_{\bullet,6}^{0.67} \left(\frac{R}{10^3 R_g} \right) \text{ g cm}^{-2}. \quad (25)$$

Although such a cool disk is geometrically thin close to a SMBH, it is still gravitationally stable: the Toomre parameter

$$Q(R) \equiv \frac{\Omega^2 h}{\pi G \Sigma} = 9 \times 10^4 \alpha^{0.33} M_{\bullet,6}^{-1.67} \left(\frac{R}{10^3 R_g} \right)^{-5/2} \quad (26)$$

is well above unity inside 10^{4-5} gravitational radii, as long as the internal disk temperature remains buffered at 10^4 K.

The development of a warp in an orbiting thin disk, including the effects of self-gravity, viscous diffusion, and the Lense-Thirring torque, has been studied by [Tremaine & Davis \(2014\)](#). The self-gravitational torque by itself overcomes the Lense-Thirring torque outside a radius

$$R_w = \left[\frac{\tilde{a}_\bullet c^2 R_g^{5/2}}{\pi G \Sigma(R_w)} \right]^{2/7}. \quad (27)$$

Here $\tilde{a}_\bullet = a_\bullet/R_g$ is angular momentum of the BH in units of GM_\bullet^2/c . Because $\Sigma(R)/R$ is constant in the range of radius where Equation (23) is valid, we have

$$\begin{aligned} \frac{R_w}{R_g} &= \left[\frac{\tilde{a}_\bullet c^2}{\pi G R_g^2 (\Sigma/R)} \right]^{2/9} \\ &= 6 \times 10^3 \alpha^{2/27} \tilde{a}_\bullet^{2/9} M_{\bullet,6}^{-10/27}. \end{aligned} \quad (28)$$

We posit that the disk outside this radius is misaligned with the spin of the SMBH. As the viscosity parameter α drops below $\sim 0.1 Q(R_w) h(R_w)/R_w$ (but is still large enough to suppress the propagation of bending waves, $\alpha \gg h(R_w)/R_w$), the equilibrium warp profile develops a strongly oscillatory component that migrates inward from $R \sim R_w$ (see Figure 8 of [Tremaine & Davis 2014](#)). For a disk at the threshold of an ionization transition, this corresponds to $\alpha \lesssim 0.2 \tilde{a}_\bullet^{-6/11} M_{\bullet,6}^{-25/22}$. This oscillatory warp rises to a large amplitude a modest distance inside radius R_w . The following discussion is based on the hypothesis that, at this stage, the disk fragments into thin annuli, an effect that is seen in numerical simulations of disks without self-gravity ([Nealon et al. 2015](#)).

5.1. Reflection by Annular Fragments of a Warped Disk

Here we consider the reflection of a light pulse from a central source by fragments of a warped disk, which are represented by axisymmetric, tilted annuli. The emitted rays have already been gravitationally lensed² by the SMBH; we are considering here their subsequent interaction with cool

² We assume that the frozen disk, which would have a very low surface density near the ISCO (Equation (25)), is present only at $R \gg R_g$.

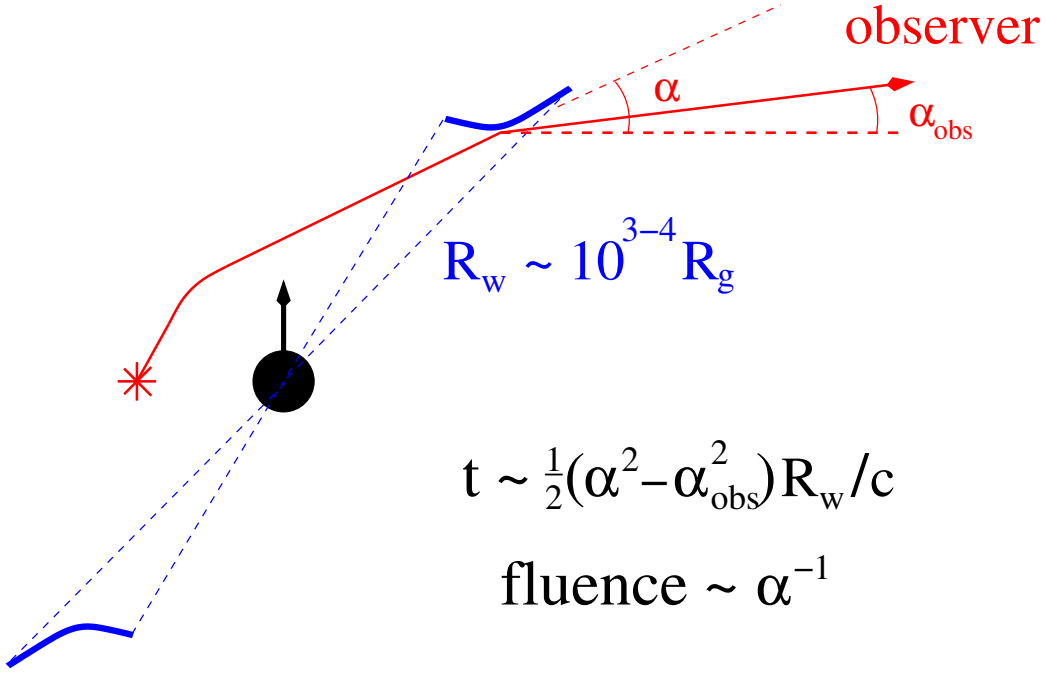


Figure 13. Rays emitted by a tiny explosion near the ISCO of a SMBH converge into a gravitational caustic in a direction nearly antipodal to the explosion site. Rays propagating near the BH equator are also reflected by annular fragments of a warped H/He disk concentrated around radius R_w given by Equation (28). Reflection produces an additional geometrical delay depending on the angular offsets α_{obs} and α from the BH equator of the observer and of the outgoing ray before reflection. Fluence transported by the ray diverges as $\sim \alpha^{-1}$, and therefore decreases with geometrical delay (relative to unreflected rays) as $\sim t^{-1/2}$ for $t > \alpha_{\text{obs}}^2 R_m / 2c$.

H/He orbiting at a fairly large distance ($R_w \sim 10^{3-4} R_g$) from the BH (Figure 13). The most strongly lensed rays travel closest to the BH equator and also are most likely to interact with a warped disk that has aligned with the BH spin well inside radius R_w .

The surface of each annulus is written in cylindrical coordinates (R, ϕ, z) aligned with the spin of the BH,

$$z_d(R, \phi) = h(R) \sin[\phi - \phi_0(R)]. \quad (29)$$

Here ϕ_0 marks the nodal line. The observer sits well beyond the reflection point in the cartesian direction \hat{x} . The outgoing ray is nearly radial just before reflection, $\hat{k} = \hat{r}$, and after reflection has unit vector

$$\hat{k}' = \hat{k} - 2(\hat{k} \cdot \hat{n}_d)\hat{n}_d, \quad (30)$$

where

$$\begin{aligned} \hat{n}_d &= n_{d,0} \left[\hat{z} - (\partial_R z_d) \hat{R} - R^{-1} (\partial_\phi z_d) \hat{\phi} \right]; \\ n_{d,0} &\equiv [1 + (\partial_R z_d)^2 + R^{-2} (\partial_\phi z_d)^2]^{-1/2} \end{aligned} \quad (31)$$

is the unit normal vector of the annulus at the reflection point $[R_{\text{ref}}, \phi_{\text{ref}}, z_d(R_{\text{ref}}, \phi_{\text{ref}})]$. Requiring \hat{k}' to lie in the direction of the observer leads to two constraints, the first on the magnitude of the

radial disk warp at the reflection point

$$\left(\frac{R}{z_d}\partial_R z_d\right)_{R_{\text{ref}},\phi_{\text{ref}}} = \frac{1}{2} [1 - (\partial_R z_d)^2 - R^{-2}(\partial_\phi z_d)^2]_{R_{\text{ref}},\phi_{\text{ref}}} \quad (32)$$

(from $\hat{k}' \cdot \hat{z} = 0$), and the second on the azimuthal angle of the reflection point

$$\tan \phi_{\text{ref}} = \left(-\frac{z_d \partial_\phi z_d}{R(R + z_d \partial_R z_d)}\right)_{R_{\text{ref}},\phi_{\text{ref}}} \quad (33)$$

(from $\hat{k}' \cdot \hat{y} = 0$). The first expression states that the radial warp must be mild. The second expression strongly limits the azimuthal offset of the reflection point from the direct line of sight between the observer and the BH: given that the nodal lines of the rings are randomly distributed in azimuth, one typically has $|\partial_\phi z_d| \sim |z_d|$. (We focus here on the case where the outer disk is moderately tilted from the equatorial plane of the BH, and not nearly perpendicular.) Except for the strongest warps and longest geometrical delays, the ray offset is small, $\phi_{\text{ref}} \sim (z_d/R)_{\text{ref}}^2$.

There is now an interesting implication for the polarization of the brightest and most strongly lensed rays. These rays reflect off disk annuli of height $z_d \ll R_{\text{ref}}$, and the reflection point, as seen by a distant observer positioned near the equator, lies nearly directly above (or below) the gravitational caustic: $\delta\phi/\delta\theta = \phi_{\text{ref}} R_{\text{ref}}/z_d \sim z_d/R_{\text{ref}} \ll 1$. In other words, the plane of reflection runs nearly in a longitudinal direction: $\hat{\theta} \cdot (\hat{k} \times \hat{k}') \simeq 0$.

In this situation, there is only a weak rotation of the polarization vector following reflection. Treating the disk surface as a conducting sheet, the unit electric vector after reflection is

$$\hat{E}' = 2(\hat{E} \cdot \hat{n}_d)\hat{n}_d - \hat{E}, \quad (34)$$

the (irrelevant) minus sign deriving from the surface boundary condition $\mathbf{E} \times \hat{n}_d \rightarrow 0$. Supposing the ray to be polarized $\hat{\phi} \cdot \hat{E} = 0$ before reflection (Figures 5, 6), the electric vector after reflection has a small azimuthal component

$$\hat{E}' \cdot \hat{y} \simeq -2 \left(\frac{\partial_\phi z_d}{R}\right)_{R_{\text{ref}},\phi_{\text{ref}}}. \quad (35)$$

Gravitational lensing enhances the ray fluence in proportion to $\alpha^{-1} \sim R_{\text{ref}}/z_d$; hence, one finds a small rotation of the polarization vector scaling inversely with the fluence of the reflected pulse.

6. APPLICATION TO REPEATING FRBS

A single FRB source, FRB 121102 (Spitler et al. 2016), is presently known to repeat. Bursts from this source sometimes arrive in clusters lasting a few hours, the best sampled of which was reported by Gajjar et al. (2018) and Zhang et al. (2018) in a 5-8 GHz band. Here we consider how a combination of gravitational lensing and reflection off annular fragments of a quiescent disk may transform a single point emission near the ISCO of a SMBH into a burst cluster of a similar duration (Thompson 2017a).

6.1. Effect of Gravitational Lensing

The pattern of repetitions produced by gravitational lensing was worked out in Sections 2.2-2.3, 3 and 4. It is possible, in principle, to measure both the mass and spin of the BH by detecting both

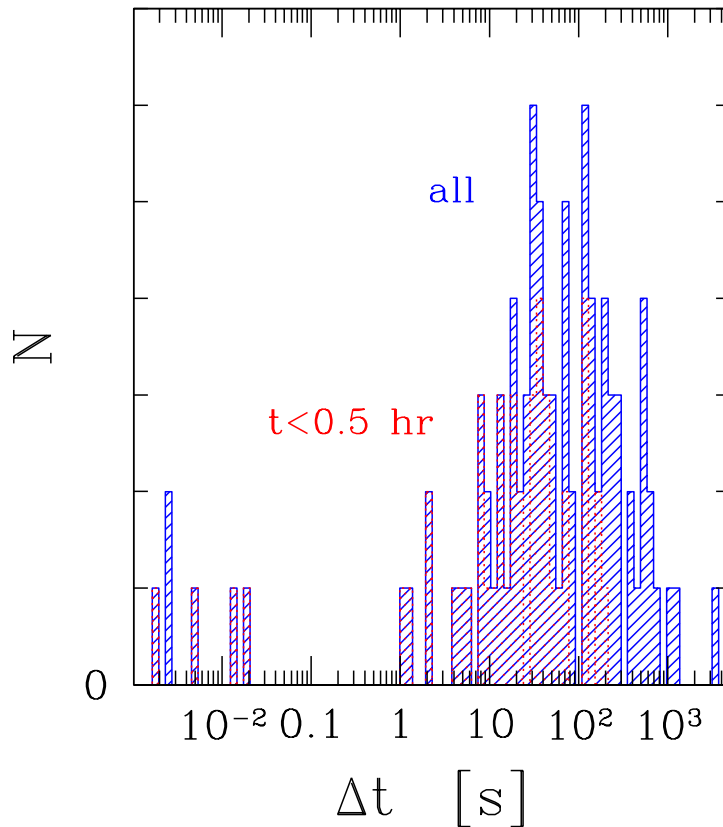


Figure 14. Histogram of intervals between successive bursts, as recorded from FRB 121102 in a single ~ 4.5 hr cluster by Zhang et al. (2018). Red histogram is the subsample of bursts arriving earlier than 0.5 hr from the start of the observation.

prograde and retrograde periodicities in the delayed pulses. Nonetheless, periodicity at fixed observer azimuth ϕ emerges only with a delay of $\sim (40 - 60) GM_{\bullet}/c^3$, depending on the spin of the BH (Figure 7), and is accompanied by exponential dimming (Figure 4). In the case of a rapidly spinning BH, around which the prograde light rays dim relatively slowly, the retrograde rays are greatly reduced in brightness compared with the prograde rays.

The first repeat pulse arrives with a delay that varies smoothly with the azimuth of the observer relative to the emission point. In the case where observer and emission are nearly antipodal, a ray caustic is observed with a characteristic delay $(5 - 10)GM_{\bullet}/c^3$ that depends on both M_{\bullet} and $\tilde{a}_{\bullet} = a_{\bullet}/R_g$ (Figure 10). The azimuth of peak brightening shifts significantly from the antipodal direction as $\tilde{a}_{\bullet} \rightarrow 1$. Given a favorable orientation relative to the BH equator, this delayed brightening might be identified after monitoring multiple burst clusters, each sourced by an explosion at a random orbital phase.

Figure 14 shows the distribution of intervals between successive bursts in the FRB 121102 cluster reported by Zhang et al. (2018). A few very rapid repetitions are observed, but then there is a large gap in repetition time up to ~ 10 s, followed by a broad distribution of intervals extending up to

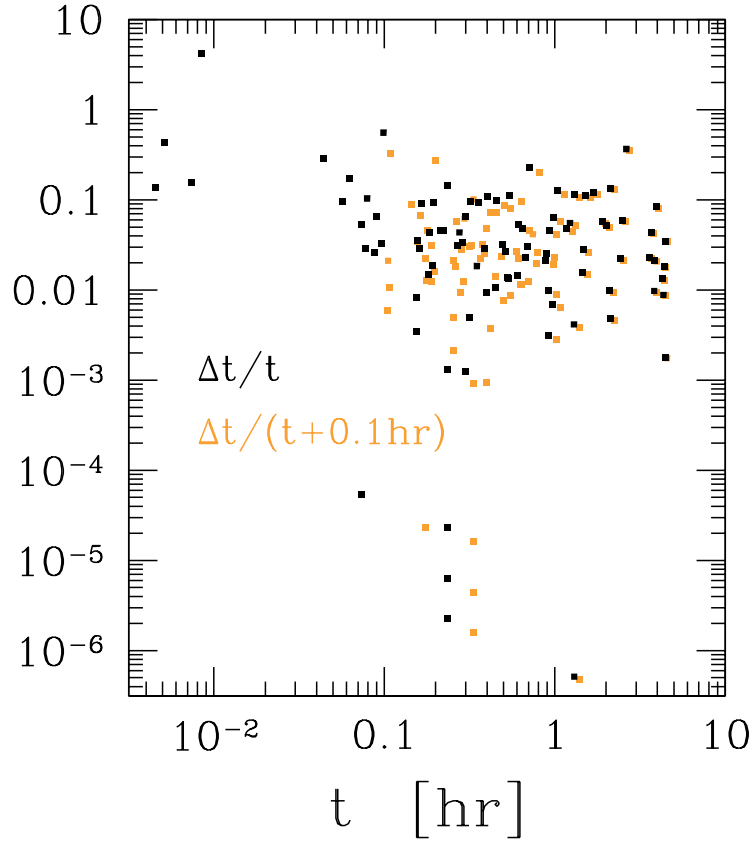


Figure 15. Black points: intervals Δt between successive bursts from FRB 121102, relative to the time t since the start of observations as recorded by Zhang et al. (2018). The source was active at the start; hence, $\Delta t/t$ is artificially enhanced at small t . Because the distribution of $\Delta t/t$ flattens at large t , we may estimate the time that the source had been active before the start of observations by adding an offset time to t . The gold points show the result for an offset of 0.1 hr.

$\sim 10^3$ s. Identifying the lower range of this broad distribution with a lensing delay of $(5-10) GM_{\bullet}/c^3$ implies a SMBH mass $M_{\bullet} = (2-4) \times 10^5 M_{\odot}$. Fast (approximately millisecond) repetitions could be produced self-consistently by the process of specular reflection, during which the pulse intensity is high enough to induce trans-relativistic motion in the plasma mirror (Thompson 2017a). The incidence of fast repetitions detected in FRBs also limits the abundance of an intervening cosmological population of 30-100 M_{\odot} BHs through the effect of gravitational lensing (Muñoz et al. 2016).

6.2. Reflection of Lensed Rays off Fragments of a Quiescent Disk

Although gravitational lensing may easily produce one or two bright repetitions, it cannot supply the large number detected in the burst clusters of FRB 121102, or the longer burst intervals – even if spin of the SBMH is nearly extremal – at least in the standard framework of Einsteinian relativity adopted here. Most of the intervals the the range $10 < \Delta t < 30$ s are concentrated during the first 0.5 hr of the same observation, whereas most of the longer intervals exceeding ~ 300 s are delayed

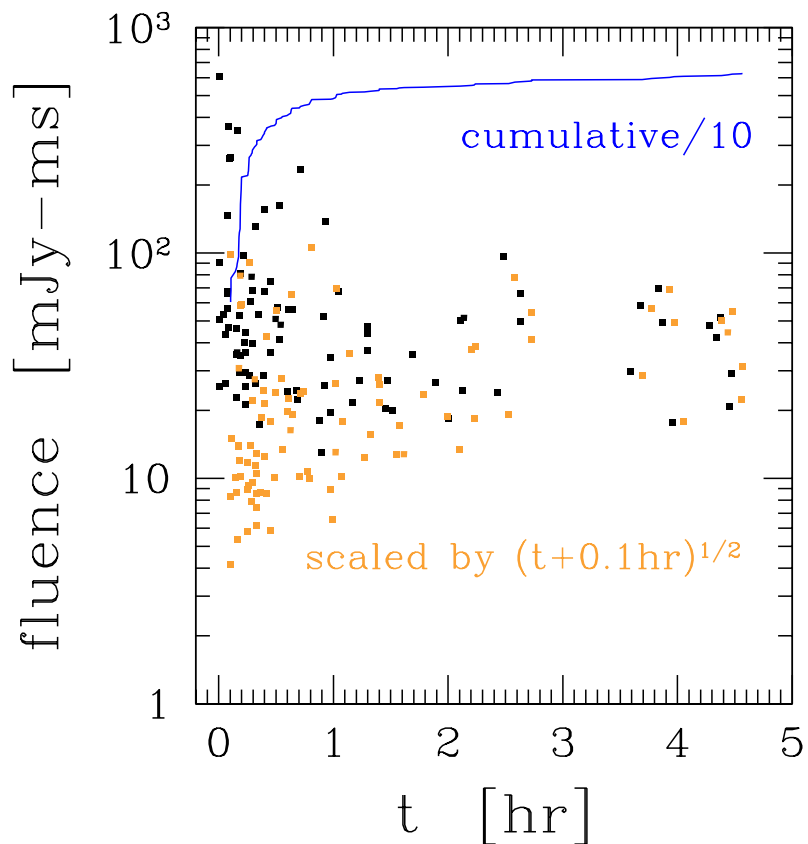


Figure 16. Dependence of burst fluence on time since the onset of observations of FRB 121102 reported by Zhang et al. (2018). Gold points compensate for the scaling $F \propto t^{-1/2}$ expected from multiple reflections of a single gravitationally lensed impulse. Gravitationally lensed burst fluence varies as $\sim \alpha^{-1}$ with angular offset α from the BH equator (Figure 3), and the delay time as $\sim \frac{1}{2}\alpha^2 R_w/c$, where $R_w \sim 10^4 GM_\bullet/c^2$ is the distance of reflecting disk fragments from the BH (Equation (28)).

to the later part (Figure 14). The ratio $\Delta t/t$ between the interval to the next burst and the time of a given burst (recorded since the beginning of the observation) is seen to have a relatively flat distribution over most of the observation (Figure 15). A rise in $\Delta t/t$ as $t \rightarrow 0$ is probably an artifact of the activation of the source at some time t_0 before the start of the observing window; this feature can be compensated by setting $t \rightarrow t + t_0$, with $t_0 \sim 0.1 - 0.3$ hr.

The flat distribution of $\Delta t/t$ is consistent with most of the repetitions being due to reflection off a large number of cool H/He clouds, here modeled as annular fragments of a thin disk, which are uniformly distributed in angle as seen from the BH. Gigahertz waves can escape from the near-horizon region only if the electron density there is low, and so any disk component of the accretion flow naturally has frozen out. As discussed in Section 5, such a quiescent disk may fragment at a distance $\sim R_w$ from the BH given by Equation (28), as a result of a competition between its self-gravity and the Lense-Thirring torque exerted by the BH.

A ray directed at angle $\alpha = \theta - \pi/2$ from the BH equator, and then scattered into a direction $\alpha_{\text{obs}} = \theta_{\text{obs}} - \pi/2$ aligned with the observer, experiences a delay $t \simeq \frac{1}{2}(\alpha^2 - \alpha_{\text{obs}}^2)R_w/c$ (Figure 13). The maximum delay $\sim R_w/c$ matches that observed in the burst cluster of Figure 14 (~ 4 hr) for $M_{\bullet} \sim 4 \times 10^5 M_{\odot}$.

6.3. *Lensing Bias and Dimming of Reflected Pulses*

FRBs emitted near the ISCO of a SMBH are predicted to be substantially brighter when the emission point is nearly antipodal to the observer (Figures 2 and 4). The detection volume of a repeating FRB source is therefore increased if the the spin of the SMBH lies in the plane of the sky (Figure 11). This opens up an interesting mechanism for producing intermittent burst activity: the source is harder to detect when the random emission phase of the seed explosion is offset from the direction antipodal to the observer. When the alignment is favorable and the burst is strongly gravitationally lensed, one also expects a negative correlation between fluence and the additional delay time(s) produced by reflection, because the fluence scales with angular offset α of the outgoing ray (before reflection) as $F \propto \alpha^{-1}$ (Figure 3). Hence

$$F(t) \propto \left(\frac{2ct}{R_m} + \alpha_{\text{obs}}^2 \right)^{-1/2}, \quad (36)$$

where α_{obs} is the offset of the observer from the BH equator. Applying the inverse of this scaling to the burst cluster of FRB 121102 significantly flattens the distribution of burst fluence with delay time (Figure 16).

One also sees from Equation (36) that lensing bias survives the addition of plasma reflection to the effects of gravitational lensing. In fact, given the tendency of the inner disk to align with the spin of the BH, it is possible that cool H/He blocks the direct line of sight between the Earth and the ISCO region of a SMBH associated with FRB 121102, so that bursts are only detected in reflection.

6.4. *Linear Polarization*

Our final consideration is the polarization of the emitted bursts. Strong linear polarization is expected for tiny electromagnetic explosions emitted near the ISCO of a SMBH, because the damping length of the injected subluminal pulse is much smaller than r_{isco} (Thompson 2017b). (By contrast, the damping length is more than $\sim 10^{13}$ cm in interstellar conditions.) This has been measured in three burst clusters of FRB 121102, which also exhibit a uniform direction of source polarization (Michilli et al. 2018).

Rays propagating near the BH equator maintain a consistent polarization direction (Figure 12) as long as the magnetic field has a persistent (toroidal or poloidal) orientation near the ISCO. The same polarization direction is shared, for SMBHs of modest spin $\tilde{a}_{\bullet} \lesssim 0.7$, by strongly lensed rays that propagate above or below the intensity cusp. The reflection of these rays off annular fragments of a quiescent disk largely preserves this polarization (Equation (35)). The alignment of the polarization is predicted to weaken in pulses with increasing delay time (and decreasing pulse fluence).

A large Faraday rotation measure is a firm prediction of emission from close to a SMBH and has been recently observed (Michilli et al. 2018). The electron density near the SMBH that allows the escape of gigahertz waves is too small to sustain a continuous jet that powers the persistent radio source reported by Chatterjee et al. (2017) and Marcote et al. (2017); instead, the persistent emission

must be powered by an outward-moving blast wave further from the hole. Such a blast would suppress accretion onto the SMBH, as is needed for radio wave escape. In this situation, the Faraday rotation measure could be dominated by material at the radius of the blast, which has been estimated to be $\sim 0.1 - 0.3$ pc in a fairly model-independent way (Beloborodov 2017; Margalit & Metzger 2018). We note that this blast dimension is small enough to be contained inside the Bondi radius of a SMBH of mass $\sim 3 \times 10^5 M_\odot$, meaning that the rotation measure will decrease with time as the material and magnetic field swept up by the shock is spread over a larger volume; there is now tentative evidence for this (Michilli et al. 2018). For example, the blast radius increases with time as $R_s \sim t^{1/2}$ when the ambient plasma density scales with distance r from the SMBH as $n_e \propto r^{-1}$. Taking the magnetic field to be the corresponding equipartition value, $B(r) \propto r^{-1}$, the rotation measure scales as $RM(R_s) \propto R_s^{-1} \propto t^{-1/2}$.

6.5. Synopsis

The same relative orientation of SMBH, emission point, and observer that results in (i) brightening of the emitted pulse by strong gravitational lensing, (ii) enhanced detectability of the source, and (iii) a $\sim t^{-1/2}$ decay of the fluence observed in independently reflected rays with different delay times, also produces (iv) a consistent direction of linear polarization in the separate ray bundles. We obtain two estimates of the mass of a SMBH host of FRB 121102; both point to $M_\bullet \sim 3 \times 10^5 M_\odot$. This is on the low end of the SMBH mass spectrum, as would be expected if the persistent radio counterpart of FRB 121102 (Chatterjee et al. 2017; Marcote et al. 2017) is a BH: this source resides in a dwarf galaxy with a low ($\lesssim 10^8 M_\odot$) stellar mass (Tendulkar et al. 2017).

7. DISCUSSION

We have calculated the time and polarization profiles of a pointlike electromagnetic explosion near a BH, as seen by an observer at a large distance. The underlying physical model involves a collision between two massive objects (magnetic dipoles in the application to FRBs) orbiting near the ISCO. Our main results are as follows.

1. The intensity and polarization profile on the sphere at infinity is calculated by ray tracing. Gravitational lensing produces a strong caustic peak in a direction nearly antipodal to the emission point (exactly for a nonspinning BH), and is also accompanied by a broader Doppler peak representing the motion of the emission frame. The fraction of the rays absorbed by the BH grows with increasing spin rate, as does the fraction of escaping rays that arrive in the form of delayed pulses.

2. The time profile shows multiple impulses at each position (θ, ϕ) on the sky, representing rays that are emitted at different angles in the emission frame. Measuring forward from the first detected impulse, there is initially no periodicity. Two distinct periods eventually emerge, representing the orbital periods of the prograde and retrograde light rings.

3. The delayed pulses produced by prograde and retrograde rays connect with each other and with polar rays at discrete azimuths. Caustics coincide with the connection points between polar and equatorial rays. The azimuth of a given caustic shifts relative to the preceding caustic of the same type (except in the case of vanishing BH spin). The decay of the fluence transmitted to a fixed observer by successive pulses agrees with the fundamental spin-1 quasi-normal mode in the Schwarzschild case, but such a comparison is complicated by the aperiodic intervention of caustic features when the BH spins.

4. We examine the polarization profile produced by emission due to the upboosting of an ambient magnetic field into a propagating superluminal transverse mode by a small explosion. The electric vector measured by an equatorial observer at a large distance from the BH maintains a fairly uniform orientation over a wide range of azimuth relative to the emission point.

5. There is an observational bias in favor of observing *repeated* electromagnetic explosions from a BH whose spin is oriented in the plane of the sky.

As for the application to FRB 121102 and other potential repeating FRB sources, we note the following.

6. Strong lensing of electromagnetic bursts emitted at random phases near the ISCO is a possible source of apparent intermittency: only if the emission point is nearly antipodal with the direction of the observer is the lensing amplification strong. Intermittent growth and decay of the accretion rate onto the hole, associated with rising and falling synchrotron absorption, could also sporadically shield gigahertz waves from detection (Thompson 2017a). These two possibilities can be distinguished by coordinated measurements at high and low frequencies.

7. Strong linear polarization is predicted for repeating FRBs, because of the short damping length of the injected energy compared with the radius of the ISCO and, therefore, compared with any plausible coherence length of the ambient magnetic field. This polarization will maintain a consistent direction if the observer lies in the equatorial plane of the SMBH, as lensing bias would suggest he or she is most likely to. It will also be maintained by plasma reflection when the burst is strongly gravitationally lensed – that is, if the emission point and the direction of the observer are nearly antipodal. A test of our approach is that any repeating FRB source must have a large Faraday rotation, a general property of the plasma around SMBHs; and, conversely, FRBs with modest measured rotation measures must not repeat.

8. Repeat bursts produced by reflection off annular fragments of a quiescent disk orbiting the SMBH around the radius given by Equation (28) will have a peak flux decaying as $\sim t^{-1/2}$ with the time since the first detected burst, once again if the emission point and the observer are nearly antipodal. A burst cluster from FRB 121102 reported by Gajjar et al. (2018) and Zhang et al. (2018) is consistent with this, and also shows a flat distribution of fractional time intervals $\Delta t/t$ between bursts.

9. More generally, the detection of repeating FRB pulses emitted from near-horizon regions of SMBHs would offer valuable probes of plasma dynamics in strong gravitational fields and would constrain departures from Einsteinian gravity or the presence of bound states of relativistic fields, such as light axions.

The author would like to thank Aaron Zimmerman for conversations, and the NSERC of Canada for financial support.

APPENDIX

A. COMPUTATIONAL PROCEDURES

We describe some details of the computation and numerical tests.

A.1. Tetrad for a Circular Orbit

A photon is emitted with 4-momentum k_{em}^a as measured in the rest frame of a massive orbiting particle, labeled ‘em’, with angular velocity given by Equation (3). This frame is connected by a Lorentz boost with the ZAMO frame rotating with angular velocity (2). This boost mixes the (0) and (3) tetrad components of the momentum, while preserving the (1) and (2) components (those parallel to \hat{r} and $\hat{\theta}$ in B-L coordinates). Hence

$$\begin{aligned} k_{\text{zamo}}^{(0)} &= \gamma_{\text{em}} (k_{\text{em}}^{(0)} + \beta_{\text{em}} k_{\text{em}}^{(3)}); & k_{\text{zamo}}^{(1,2)} &= k_{\text{em}}^{(1,2)}; \\ k_{\text{zamo}}^{(3)} &= \gamma_{\text{em}} (k_{\text{em}}^{(3)} + \beta_{\text{em}} k_{\text{em}}^{(0)}), \end{aligned} \quad (\text{A1})$$

where β_{em} is given by Equation (7). The 4-momentum in the ZAMO frame is constructed from the ray tangent vector measured in the B-L frame as

$$\begin{aligned} k_{\text{zamo}}^{(0)} &= (-\tilde{g}_{tt})^{1/2} \frac{dt}{d\lambda}; \\ k_{\text{zamo}}^{(3)} &= g_{\phi\phi}^{1/2} \left(\frac{d\phi}{d\lambda} - \omega \frac{dt}{d\lambda} \right); \\ k_{\text{zamo}}^{(1)} &= g_{rr}^{1/2} \frac{dr}{d\lambda} = k_{\text{em}}^{(1)}; & k_{\text{zamo}}^{(2)} &= g_{\theta\theta}^{1/2} \frac{d\theta}{d\lambda} = k_{\text{em}}^{(2)}. \end{aligned} \quad (\text{A2})$$

Equating expressions (A1) and (A2) gives the tetrad (6).

A.2. Christoffel Symbols and Riemann Tensor for Kerr Spacetime

The Christoffel symbols corresponding to the metric (1) are tabulated in Equation (2.14) of Muller & Grave (2009). The Riemann tensor is constructed using the Carter (1973) tetrad, $R_{\mu\nu\rho\sigma} = e_\mu^a e_\nu^b e_\rho^c e_\sigma^d R_{abcd}$, where

$$\begin{aligned} e_\mu^{(0)} dx^\mu &= \left(\frac{\Delta}{\Sigma} \right)^{1/2} (dt - a \sin^2 \theta d\phi); & e_\mu^{(1)} dx^\mu &= \left(\frac{\Sigma}{\Delta} \right)^{1/2} dr; \\ e_\mu^{(2)} dx^\mu &= \Sigma^{1/2} d\theta; & e_\mu^{(3)} dx^\mu &= \frac{\sin \theta}{\Sigma^{1/2}} [adt - (r^2 + a^2)d\phi], \end{aligned} \quad (\text{A3})$$

and the tetrad components of the Riemann tensor are

$$\begin{aligned} R_{0101} &= -R_{2323} = -2R_1; & R_{0202} &= R_{0303} = -R_{1212} = -R_{1313} = R_1; \\ R_{0123} &= 2R_2; & R_{0213} &= -R_{0312} = R_2. \end{aligned} \quad (\text{A4})$$

Here

$$\begin{aligned} R_1 &\equiv \frac{Mr}{\Sigma^3} (r^2 - 3a^2 \cos^2 \theta); \\ R_2 &\equiv -\frac{aM \cos \theta}{\Sigma^3} (3r^2 - a^2 \cos^2 \theta). \end{aligned} \quad (\text{A5})$$

This construction has been tested by computing $R_{\mu\nu\rho\sigma}$ directly from the Christoffel symbols.

A.3. Testing Solutions to the Geodesic Equation

Two numerical tests of the correctness of the geodesic solution are easily available. The tangent vector must satisfy the null equation $g_{\mu\nu}(dx^\mu/d\lambda)(dx^\nu/d\lambda) = 0$; and a ray trajectory without radial or angular turning points is easily compared with the solution obtained by direct quadrature, using the integrals \mathcal{E} , \mathcal{L}_z combined with the Carter constant \mathcal{Q} . For a ray originating on the equatorial plane,

$$\mathcal{Q} = g_{\theta\theta} \left(\frac{d\theta}{d\lambda} \right)^2. \quad (\text{A6})$$

The t and ϕ components of the tangent vector are obtained from the integrals (10), and the other components satisfy the equations (Frolov & Novikov 1998)

$$\begin{aligned} \Sigma \frac{dr}{d\lambda} &= \pm R(r)^{1/2}; & R &\equiv [\mathcal{E}(r^2 + a^2) - \mathcal{L}_z a]^2 - \Delta [\mathcal{Q} + (\mathcal{L}_z - a\mathcal{E})^2]; \\ \Sigma \frac{d\theta}{d\lambda} &= \pm \Theta(\theta)^{1/2}; & \Theta &\equiv \mathcal{Q} - \cos^2 \theta \left(\frac{\mathcal{L}_z^2}{\sin^2 \theta} - a^2 \mathcal{E}^2 \right). \end{aligned} \quad (\text{A7})$$

B. COMPARING MONTE CARLO METHOD WITH SOLUTION TO FOCUSING EQUATION

Two methods can be compared for evaluating the ray fluence on the rotational equator of the BH, projected onto the sphere at infinity: first, a straightforward Monte Carlo technique and, second, an evaluation of the ray expansion starting from a small sphere surrounding the emission point, using the Raychaudhuri equations (17). Figure 17 shows excellent agreement, thereby supplying a nontrivial test of both methods. It should also be noted that, although the ray expansion is calculated for purely equatorial orbits, the caustics seen in Figure 17 can be captured by the Monte Carlo technique only by including nonequatorial orbits. The method of Section 3, which integrates through singularities of the focusing equation by combining the expansion with the one nonvanishing component of the ray shear tensor, is specialized to equatorial orbits.

REFERENCES

- Bardeen, J. M., Press, W. H., & Teukolsky, S. A. 1972, *ApJ*, 178, 347
- Bardeen, J. M., & Petterson, J. A. 1975, *ApJL*, 195, L65
- Beloborodov, A. M. 2017, *ApJL*, 843, L26
- Berti, E., Cardoso, V., & Starinets, A. O. 2009, *Classical and Quantum Gravity*, 26, 163001
- Blandford, R. D. 1977, *MNRAS*, 181, 489
- Bozza, V. 2008, *PhRvD*, 78, 063014
- Broderick, A. E., & Loeb, A. 2005, *MNRAS*, 363, 353
- Carter, B. 1973, *Black Holes (Les Astres Occlus)*, Eds. C. DeWitt and B. DeWitt, (New York: Gordon and Breach), p. 57
- Chatterjee, S., Law, C. J., Wharton, R. S., et al. 2017, *Nature*, 541, 58
- Cunningham, C. T., & Bardeen, J. M. 1972, *ApJL*, 173, L137
- Dokuchaev, V. I., & Nazarova, N. O. 2017, *Soviet Journal of Experimental and Theoretical Physics Letters*, 106, 637
- Frolov, V. P., & Novikov, I. D. 1998, *Black hole physics: basic concepts and new developments* (Dordrecht: Kluwer Academic)
- Gajjar, V., Siemion, A. P. V., Price, D. C., et al. 2018, *ApJ*, 863, 2
- Gammie, C. F. 1996, *ApJ*, 457, 355
- Gralla, S. E., Lupsasca, A., & Strominger, A. 2018, *MNRAS*, 475, 3829
- Hindmarsh, A. C. 1983, *IMACS Transactions on Scientific Computing*, eds. R. S. Stepleman et al. (Amsterdam: North-Holland), p. 55

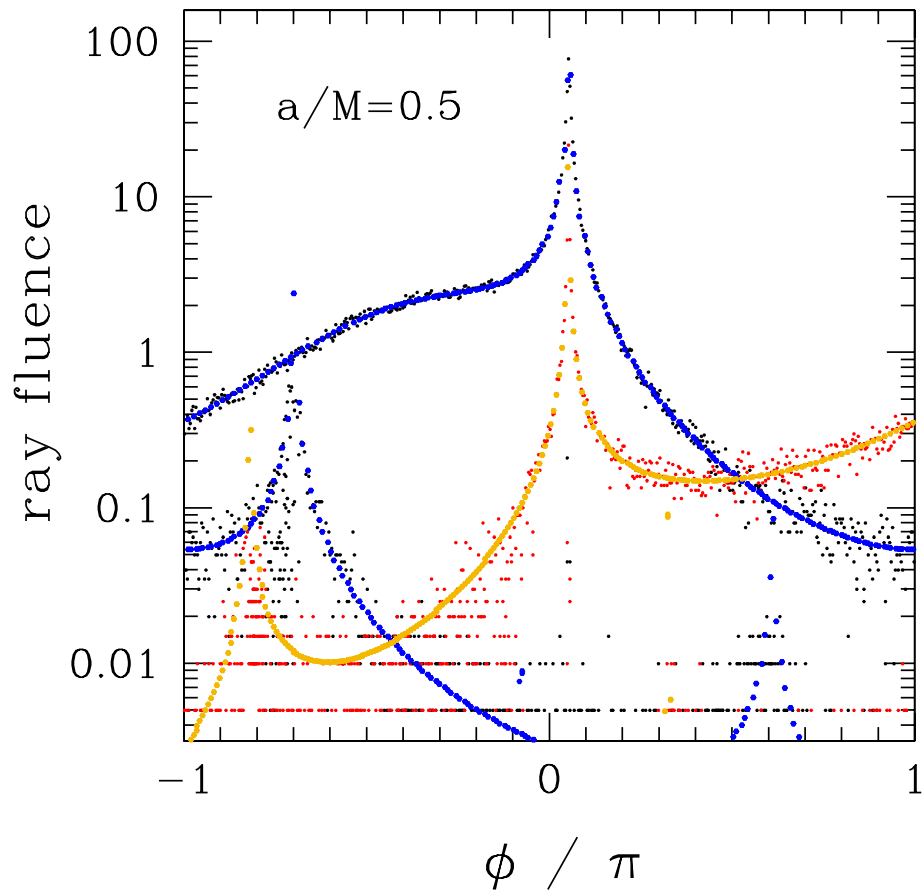


Figure 17. Large points (blue and gold): solution to the Raychaudhuri equations (17) for a BH with spin $a/M = 0.5$, as a function of the azimuth of the ray at a large distance from the BH. Small scattered points (black and red): ray fluence as calculated by a Monte Carlo technique with 2^{23} rays and angular cells of size $\Delta\theta = 2^{-8}\pi$ and $\Delta\phi = 2^{-8}(\sin\theta)^{-1}\pi$. Black and blue points: prograde photon orbits; red and gold points: retrograde orbits.

- Marcote, B., Paragi, Z., Hessels, J. W. T., et al. 2017, *ApJL*, 834, L8
- Margalit, B., & Metzger, B. D. 2018, arXiv:1808.09969
- Michilli, D., Seymour, A., Hessels, J. W. T., et al. 2018, *Nature*, 553, 182
- Müller, T., & Grave, F., arXiv:0904.4184
- Muñoz, J. B., Kovetz, E. D., Dai, L., & Kamionkowski, M. 2016, *Physical Review Letters*, 117, 091301
- Nayakshin, S., & Sunyaev, R. 2003, *MNRAS*, 343, L15
- Nealon, R., Price, D. J., & Nixon, C. J. 2015, *MNRAS*, 448, 1526
- Pacholczyk, A. G. 1970, *Radio Astrophysics* (San Francisco: Freeman)
- Poisson, E. 2004, *A relativist's toolkit: the mathematics of black-hole mechanics*, (Cambridge: Cambridge University Press)
- Pringle, J. E. 1981, *ARA&A*, 19, 137
- Rauch, K. P., & Blandford, R. D. 1994, *ApJ*, 421, 46
- Rees, M. J. 1977, *Nature*, 266, 333
- Spitler, L. G., Scholz, P., Hessels, J. W. T., et al. 2016, *Nature*, 531, 202
- Tendulkar, S. P., Bassa, C. G., Cordes, J. M., et al. 2017, *ApJL*, 834, L7
- Thompson, C. 2017a, *ApJ*, 844, 65
- Thompson, C. 2017b, *ApJ*, 844, 162
- Tremaine, S., & Davis, S. W. 2014, *MNRAS*, 441, 1408
- Weinberg, S. 2008, *Cosmology* (Oxford: Oxford University Press)
- Zenginoğlu, A., & Galley, C. R. 2012, *PhRvD*, 86, 064030
- Zhang, Y. G., Gajjar, V., Foster, G., et al. 2018, arXiv:1809.03043
- Zhu, Z., Hartmann, L., & Gammie, C. 2009, *ApJ*, 694, 1045